Effect of Solar Farms on Soil Erosion in Hilly Environments: A Modeling Study from the Perspective of Hydrological Connectivity

Hu Liu[1,2,3], Chuandong Wu[1,2,3], Yang Yu[4], Wenzhi Zhao[1,2], Jintao Liu[5] , Hailong Yu[6], Yanli Zhuang[1,2], Omer Yetemen[7]

[1] Linze Inland River Basin Research Station, Chinese Ecosystem Research Network, Lanzhou 730000, China
[2] Northwest Institute of Eco-Environment and Resources, Chinese Academy of Sciences, Lanzhou 730000, China
[3] University of Chinese Academy of Sciences, Beijing 100029, China
[4] School of Soil and Water Conservation, Beijing Forestry University, Beijing 100038, China
[5] State Key Laboratory of Hydrology-Water Resources and Hydraulic Engineering, Hohai University, Nanjing 210098, China
[6] School of Geography and Planning, Ningxia University, Yinchuan 750021, China
[7] Eurasia Institute of Earth Sciences, Istanbul Technical University, Maslak, Istanbul 34469, Turkey

Corresponding author: Hu Liu (lhayz@lzb.ac.cn)

Key Points:

- Precipitation property and relief amplitude are major controlling factors for soil erosion in utility-scale solar farms in hilly areas.
- Utility-scale solar farms could increase soil erosion mainly by increasing runoff and local hydrological connectivity.
- Higher background hydrological connectivity could aggravate the effects of Utility-scale solar farms on soil erosion.

Abstract

Compared to the growing number of utility-scale solar farms (USFs) sitting in hilly regions, knowledge of the hydrological behaviors in responding to the installation of USFs in these environments remains limited. We present herein a novel model (the Solar-Farm model) to understand the hydrological behaviors following the construction of a USF in the Loess Hilly Region of China, by combining it with an index of hydrological connectivity (HC). Scenarios were designed to estimate the effects of climate and terrain in controlling the effects of the USF on soil erosion, by altering the mean annual precipitation amount, the frequency of precipitation events, and the relief amplitude. Our results show that land use changes (e.g., vegetation removal) incurred a considerable increase in the accumulative soil erosion (22.45%-66.48%) during the installation period. During the 40-year deployment period, photovoltaic panels (PVs) incurred an average of 0.138 m deeper erosion in the USF compared with the background rate without PVs. A wetter climate induced the highest increase (88.25%) in erosion. However, the relief amplitude and precipitation frequency are also confirmed as important controlling factors for soil erosion (increased by 58% and 85.42%, respectively). The HC was increased during both the construction (0.005-0.12) and operation periods (0.149-0.314). Correlation analysis presented that the landscapes with higher HC were more likely to be exposed to the risks of soil erosion. USFs could increase soil erosion by increasing runoff and local HC, and higher background HC in turn could further aggravate the effects of USFs on soil erosion.

1 Introduction

As an alternative to conventional fossil fuels, renewable energy (e.g., solar, wind, hydropower etc.) is becoming the primary means of meeting energy demand (Dhonde et al., 2022; Makaronidou, 2020). Comparing all the renewable types, based on environmental, economic, and safety criteria, solar energy appears to be the most promising and attractive one (Bórawski et al., 2019). However, solar farms have a large land footprint (Rahman et al., 2022), and the unprecedented growth of utility-scale solar farms (USFs, defined as solar farms with nameplate generating capacity larger than 5 MW (Kruitwagen et al., 2021)) creates potential conflicts with other land uses (e.g., agriculture, pasture, industry or settlements) (Dhonde et al., 2022), and thus raises the issue of land cost (Lee, 2019; Randle-Boggis et al., 2020). Accordingly, an ever-growing number of USFs have to find homes on cheaper land such as hilly terrain and lower mountain slopes (Chiabrando et al., 2009; Makaronidou, 2020). However, mounting USFs in these environments also incurs disadvantages, including increased stormwater runoff, soil erosion (Figure S1), and sediment transport (Cook and McCuen, 2013), which in turn pose considerable threats to the local and surrounding environments (Belding et al., 2020; Bolinger and Seel, 2018). This is even more likely to be the case in regions where storms occur often, vegetation cover is low, and soil is easily lost (e.g., Loess Plateau in China) (Yu et al., 2020). Accordingly, it is of extreme importance to understand the potential effects of USFs (both existing and proposed) on hydrological behaviors in hilly regions (Phalane, 2021), for better designing and managing the USFs toward sustainable development (Cook and McCuen, 2013; Makaronidou, 2020).

Given the rare *in situ* and long-term field observations available at most USFs around the world, modeling is currently the only practical option for achieving this end (Baartman et al., 2018; Cabal et al., 2021). PV-affected hydrological behaviors in USFs have been investigated in a few previous studies (Chiabrando et al., 2009). For example, Walston et al. (2021) reported significantly increased sediment and water retention at USFs across the Midwestern USA; Cook and McCuen (2013) concluded that whether the addition of photovoltaic panels (PVs) affects hydrological processes depends largely on whether there are changes in the land-cover type under the PVs; Edalat (2017) reported that an increase in the tilt angle of PVs results in decreases in peak flow, peak flow time, and runoff. These works, however, were limited in the sense that they did not consider the co-evolution of soil and vegetation under the impact of PVs over the life-span of a USF. Indeed, PVs may significantly change microclimates (i.e., solar radiation and rainfall), so that soil and vegetation in USFs could more intensely co-evolve to adapt to the altered environments during the long running period (Hernandez et al., 2014; Makaronidou, 2020). The limitation of overlooking the long-term co-evolution effects might lead to unexpected bias in the predictions of the hydrological responses to the shift in land uses, especially when USFs are installed in hilly environments. However, how to evaluate the hydrological behaviors in response to the installation of USFs during their long operational period remains a challenge (Hernandez et al., 2015; Murphy-Mariscal et al., 2018).

Addressing the above-noted issues requires solutions that offer flexibility and robustness in dealing with the coupling between ecohydrological processes and landscape development: e.g., the extent and distribution of expected effects of PVs on the processes of rainfall runoff and erosion deposition

as they occur over the life-span of USFs in hilly environments (Wacha et al., 2018). The concept of hydrological connectivity (HC) depicts "water-mediated transport of matter, energy and/or organisms within or between elements of the hydrologic cycle" (Pringle, 2001), and thus appears to be a likely solution (Bracken and Croke, 2007; Souza and Hooke, 2021). Using this concept, previous works have evaluated the potential hydrological and environmental impacts of altered ground surface conditions from vegetation dynamics (Foerster et al., 2014; Souza and Hooke, 2021), biological conservation (Pringle, 2001), land use changes (Boix-Fayos et al., 2007), water resource development (Higgisson et al., 2020), surface mining activities, and so on (Freeman et al., 2007; Kompanizare et al., 2018). Given the potential of HC in bridging the interface between ecohydrology and landscape evolution, and combining the index of HC with a model that could coordinate biotic and abiotic effects caused by PVs on vegetation dynamics, may allow us to better evaluate the long-term hydrological behaviors in USFs in hilly environments.

We present herein a water-carbon coupled model (the Solar-Farm model, SOFAR) with this property, and the long-run effects of PVs on hydrologic response in USFs will be estimated and analyzed from the perspective of HC through the model. Through these efforts, this work aims to analyze the potential erosion and runoff that can come from long-term deployment of USFs and reveal how a solar farm affects soil erosion, by highlighting the dynamic nature of HC and soil erosion due to USF deployment (Jahanfar et al., 2019). This work also discusses storm-water management strategies that can prevent potential erosion as well as runoff in USFs deployed in hilly environments, from the perspective of HC (Souza and Hooke, 2021). The presented modeling scheme provides a novel method to predict soil erosion affected by USFs in hilly regions, and a potential tool to identify the erosion-risk areas in such USFs as well. The findings will also contribute to an improved understanding of the hydrological responses to USF installation and development in hilly regions, and ultimately facilitate decisions on USF siting and management both in the Chinese Loess Plateau and elsewhere.

2 Materials and Methods

2.1 Site Description

This study was carried out at the Hongsibu solar farm (37°61'N, 106°12'E; 1350 m a.s.l.) located in a hilly landscape (part of the Yellow River Basin, administratively belonging to Wuzhong, China) at an elevation of 1240–1450 m, in the Loess Plateau of China (Figure 1a) (Zhang et al., 2021). This area has a typical temperate continental arid climate with an annual average temperature of 9.2 °C (maximum daily temperature of 29.7 °C and minimum daily temperature of -14.2 °C). The average annual precipitation is approximately 186 mm, average annual evaporation is about 2387 mm, and average annual wind speed is about 2.9–3.7 m s^{-1} based on the last 38 years of available meteorological records (1980-2017 inclusive). The annual sunshine duration is up to 2900-3550 h with total solar radiation of 4936-6119 MJ m^{-2} yr^{-1}). The rainfall scarcity combined with abundant sunlight implies that this region has extensive potential for solar energy production (Guan et al., 2020). A large number of USFs have been built in this region, and the cumulative installed capacity of solar power had reached 7.81 GW by the end of 2020 (Sun et al., 2021; Tang and Low, 2020). The

terrain in this region is hilly but not mountainous, and the predominant vegetation is mixed-shrub communities including *Populus L.*, *Zygophyllaceae*, *Ulmusglaucescens*, *Leguminosae*, *Elaeagnaceae*, and so on (Zhang et al., 2022). The soil in this region exhibits a sandy loam texture (50% clay, 30% silt, and 20% sand). The main land use of the region is rural and consists predominantly of grazing—i.e., dry farm land.

The solar farm where we conducted the study was built in 2016 with an installation capacity of 200 MW. Native shrublands were cleared and leveled to the local terrain slope in order to build the solar farm. Solar modules were installed above the ground, and the disturbed ground was naturally recolonized by native grasses during the years following the installation. Given the large area and rugged terrain, we selected only the northwest area of the solar farm (about 27 MW of generating capacity) with relatively uniform soil texture and significant topographical variation, for detailed study (Figure 1b). This section (hereinafter referred to as the 'Hongsibu site') covers an area of 232 hectares of land, and consists of about 77 hectares of solar modules mounted on a racking system. Three adjacent sub-catchments (T1 to T3; the PVs in each of them have a power rating of approximately 5 MW) can be delineated from the digital elevation model within the Hongsibu site (Figure 1b and Table 1). The PVs are arranged in east–west-orientated rows and inclined southward at a tilt angle of 36.2°, and the length and width of a single photovoltaic array (which consists of two sub-panels with a 3-cm gap between them) are 4 m and 1 m, respectively (Figure 1c). Onsite vegetation is maintained through sheep grazing or irregular mowing (less than once a year) as with many other solar farms in arid northwestern China (Wu et al., 2022).

2.2 Data Acquisition

The meteorological data from 1980 to 2016 (daily maximum and minimum air temperature, sunshine duration, and total precipitation, used to run the SOFAR model) (Ren et al., 2021), observed at the Wuzhong weather station—which is about 40 km away from the solar farm (Figure 1a) —were obtained from the National Meteorological Science Data Center, China. The Wuzhong weather station and the Hongsibu site are close enough to each other—especially when considering the open and uniform landscapes (topography, vegetation, etc.) in this region—that they experience very similar weather conditions and share almost the same surface conditions. Accordingly, historical records from the Wuzhong weather station represent reasonably well the weather conditions of the Hongsibu site. The thirty-eight years of observations were input to a weather generation model (WeaGETS) (Chen et al., 2012), to stochastically generate a 50-year climate time series. Further, increased rainfall variability scenarios were produced through replacing local precipitation frequency (i.e., dry and wet period in the WeaGETs) with that of other weather station usually experienced torrential events and unpredictable droughts. Micrometeorological and soil-moisture data (from 27/04/2021 to 17/09/2022) at the site were collected using automatic weather stations and moisture sensors, and used to calibrate the SOFAR model. Four miniature weather stations were installed 50 cm above the ground at different positions beneath the PVs (i.e., Front, Middle, and Gap, according to water and light conditions), and the natural bare zone (set as Control) to measure the near-surface microclimates, including air temperature, relative humidity, precipitation, and wind velocity and direction. The volumetric soil moisture profiles (eight in total) were measured with a Time-Domain Transmissometer (TDT) (Acclima SDI-12, USA) at each zone (including the Control) and in-

between positions (except for the Control); the probes were installed at four depths below the soil surface (10, 20, 40, and 60 cm) in each profile, and data were collected at 10-min scan intervals. The reference monitoring site (Control, with shrubs of short height, i.e., 0.2-0.5 m) was located in an open space approximately 100 m away from the PVs, so that it was assumed not affected by the PVs (Figure 1a). The VWC and meteorological observations were used to validate the model parameters. Furthermore, the fine landscape characteristics of the Hongsibu site (i.e., digital elevation model, DEM) were obtained from unmanned aerial vehicle photogrammetry and ground surveys. The obtained DEM was then input into the SOFAR model for running the soil erosion processes.

2.3 Model Structures and Parameters

2.3.1 The SOFAR Model

The Solar-Farm model (SOFAR) describes the fundamental physical and ecohydrological processes occurring in a solar farm at a daily time step, including rainfall concentration, radiation harvesting, soil moisture dynamics, vegetation evolution, and landscape erosion (Figure 2a), which are driven by daily meteorological variables including precipitation, maximum temperature, minimum temperature, and sunshine duration. Compared to other modeling studies—for example, Elamri et al. (2018) only focused on the rainfall interception of PVs, and Jahanfar et al. (2020) just focused on radiation reduction—the salient aspect of SOFAR is the explicit treatment of both rainfall concentration and radiation harvesting in solar farms. However, it is challenging to simulate the rainfall harvest of PVs at the mesoscale, because the width of soil affected by this harvest is usually less than 30 cm, along the incline direction of PVs. Accordingly, coarse spatial resolution is not capable of capturing this change at such a fine scale. Furthermore, it is time-consuming and there is a high requirement of calculation capacity, if a uniform and high spatial resolution scheme is adopted. As Figure 2b shows, two spatial scales were considered in the model: farm-level (3 m × 3m) and panel-level (0.1 m × 0.1 m), in order to obtain a trade-off between accuracy and efficiency. Specifically, the locations of the PVs were identified before running the model, and local refined grids (Figure 2b) were then employed at the grids with PVs. Finally, the panel-level results were averaged and integrated into the farm-level results, which are focus of this study.

A schematic diagram of the co-evolution of soil moisture, vegetation and landscape is presented in Figure 2. The frequent exchange of matter and energy, between soil and plant, is a complex and intricate relationship. Landscape erosion rates are mainly affected by runoff and vegetation biomass, and runoff also has a significant effect on soil moisture dynamics and the water availability of plants. Runoff, though, can be affected by changes in the elevation of the landform caused by soil erosion. Nevertheless, water stress is considered the overwhelming factor in how the soil regulates plant growth, while plants affect soil moisture dynamics by regulating infiltration and evapotranspiration.

(1) Soil moisture dynamics

In the SOFAR model, the soil moisture dynamics were simulated using a bucket concept, following the general scheme described in Rodriguez-Iturbe (2000). The root-zone average soil water balance equation is described as Eq. (1), which is solved using the finite difference method.

$$nZ_r\frac{\partial S}{\partial t} = P - I - R - E(S, LAI) - T(S, LAI) + \frac{\partial K(S)}{\partial S} \quad (1)$$

where n represents the soil porosity, Z_r (mm) is the effective root depth, S is the average relative volumetric water content of the soil profile, t (d) is the time step, P (mm) is the daily precipitation amount, I (mm) is the canopy interception loss, R (mm d^{-1}) represents the drainage runoff, T (mm d^{-1}) is the actual daily transpiration, E (mm d^{-1}) is the actual evaporation from soil, and hydraulic conductivity K (cm h^{-1}) is a function of soil moisture content and saturated hydraulic conductivity (K_S, cm d^{-1}).

$$K(S) = K_s\left(\frac{S}{S_{fc}}\right)^{N+b+3} \quad (2)$$

where S_{fc} (v v^{-1}) is the field water content, and the constants N and b are empirical coefficients.

The amount of infiltration (I_a)—the effective precipitation—is restricted by three factors: available water, infiltration capacity, and available pore space in the root zone (Yetemen et al., 2015).

$$I_a = min\{P - I + R_{in}, I_c, nZ_r(1 - S)\} \quad (3)$$

where R_{in} (mm) is the runoff from upstream sources.

Vegetation enhances soil infiltration capacity through increasing pore structures, as has been verified by field experiments and modeling studies (Dunne et al., 1991). Therefore, infiltration capacity (I_C), accounting for the effects of both soil characteristics and plant dynamics, is expressed as the weighted average of I_C of bare soil (I_b) and a fully averaged surface (I_V). In Eq. 6, the vegetation cover rate (V_t) (Yetemen et al., 2015) is derived by *LAI*.

$$I_c = I_b(1 - V_t) + I_V V_t \quad (4)$$

$$V_t = 1 - \exp(-0.75LAI_t) \quad (5)$$

Surface runoff depth (mm) is expressed as a mass balance between precipitation, canopy interception, infiltration, and runoff from upstream sources.

$$R_{out} = P - I - I_a + R_{in} \quad (5)$$

(2) Roof effects of PVs

The roof effects of PVs are several. The photovoltaic panels concentrate rainfall along their downslope edges, resulting in a downpour at those locations; the panels harvest radiation, causing a radiation reduction of about 67~90% (Armstrong et al., 2016; E.Tanner et al., 2020; Liu et al., 2019); and the panels shade the subsurface soil. To capture the roof effects of PVs, the AVrain model (Agrivoltaic Plot Rain Redistribution Model, proposed by (Elamri et al., 2018)) was coupled into the SOFAR model to estimate the rainfall intercepted by the PVs and the related concentration of the rainfall process. The details of the method adopted in the SOFAR model to estimate the radiation harvested by the PVs are described in Wu et al. (2022), and are illustrated in the Appendix A.

Rainfall concentration. In the model, the irregular flow of water above the PVs is simplified to a homogeneous downward flow, and the output rainfall is concentrated on an area of 0.15 m width covering the edge of the photovoltaic panel. The incidence angle (α_{rain}) and the interception of rainfall are given by

$$\tan(\alpha_{rain}) = V_W/V_D \quad (6)$$

$$I_{PVs} = P[\cos(\beta) - \tan(\alpha_r)\sin(\beta)]K_p \quad (7)$$

where α_{rain} represents the incidence angle of the rainfall with respect to the vertical direction, V_W (m s^{-1}) is the average velocity of the wind at the site, V_D (m s^{-1}) is the velocity of the raindrops, I_{PVs} (mm) is the amount of rainfall intercepted by the PVs, β represents the inclination angle of the PV, and parameter K_P is the area coefficient (the ratio of the area of the PV to the area of the narrow drip zone), which represents the process of the PVs' concentrating rainfall into a narrow area.

Radiation harvest. Different from natural surfaces, a part of the radiation absorbed by PVs is transformed into electricity. According to the energy balance equation, the available radiation of the area beneath a PV (I_s) is given by

$$I_s = I_{PV}(1 - \varepsilon - \alpha_{PV})\eta + I_{ds} \quad (8)$$

where I_{PV} represents direct radiation incident on the surface of the PV; ε is the energy transformation efficiency of the photovoltaic panel, which is 0.18; α_{PV} is the albedo of the PV's surface, equal to 0.1; η is the PV's re-radiation coefficient; and I_{ds} is the available diffuse radiation of the sheltered area.

(3) Evaporation and transpiration

The total evapotranspiration from a fragmented landscape is calculated as the sum of the soil evaporation and canopy transpiration. The potential transpiration (T_{max}, mm d^{-1}) and evaporation (E_{max}, mm d^{-1}) are calculated through the Penman-Monteith equation, modified with the canopy coverage of green leaves (f_g) and percentage cover of bare soil (f_s) referring to the separation method described in Nouvellon et al. (2000), respectively.

$$T_{max} = f_g \frac{\Delta(R_a - G) + \rho_a c_p(e_s - e_a)/r_{ac}}{\lambda[\Delta + \gamma(1 + r_{sc}/r_{ac})]} \quad (9)$$

$$E_{max} = f_s \frac{\Delta(R_a - G) + \rho_a c_p(e_s - e_a)/r_{as}}{\lambda[\Delta + \gamma(1 + r_{ss}/r_{as})]} \quad (10)$$

where R_a (MJ m^{-2} d^{-1}) is the extraterrestrial radiation, G (MJ m^{-2} d^{-1}) represents the daily soil heat flux, (e_s-e_a) represents the vapor pressure deficit of the air, ρ_a (kg m^{-3}) is the average air density measured at constant pressure, c_p (MJ kg^{-1} $°C^{-1}$) is the specific heat of air at a constant pressure, Δ is the slope of the saturated vapor pressure curve at air temperature T_a, r_{sc} and r_{ss} are the surface resistances for a full canopy and bare soil, respectively, and r_{ac} and r_{as} are the corresponding aerodynamic resistances for canopy and bare soil, respectively.

The dependence of daily transpiration loss (T_a, mm d^{-1}) on soil moisture is expressed as a piecewise function (Laio et al., 2001), wherein transpiration is equal to zero, because stomata are fully closed when the soil moisture content drops below the wilting point (S_w).

$$T_a = \begin{cases} T_{max}, & S^* < S < 1 \\ T_{max}\dfrac{S - S_w}{S^* - S_w}, & S_W < S < S^* \\ 0, & 0 < S < S_w \end{cases} \quad (11)$$

where S^* represents the soil moisture threshold level for a plant when it starts to reduce transpiration under water stress (Srivastava et al., 2021). Just as for transpiration loss, evaporation loss from the soil is given by

$$E_a = \begin{cases} E_{max}, & S^* < S \le 1 \\ E_{min} + (E_{max} - E_{min})\dfrac{S - S_w}{S^* - S_W}, & S_w < S \le S^* \\ E_{min}\dfrac{S - S_h}{S_w - S_h}, & S_h < S \le S_w \\ 0, & 0 < S \le S_h \end{cases} \quad (12)$$

where E_{min} (mm d^{-1}) is the minimum soil evaporation, and S_h is the hygroscopic point.

(4) Vegetation growth

For the sake of simplicity of the model, the biomass of the whole plant is divided into three biomass pools: living aboveground biomass (B_{ag}), standing dead biomass (B_{ad}) (e.g., withered leaves and dead branches), and living root biomass (B_r) (Nouvellon et al., 2000). The dynamics of the three biomass pools are described as following differential equations with respect to daily time step:

$$\frac{dB_{ag}}{dt} = (1 - a_r)P_g + T_{ra} - R_{at} - S_a \quad (13)$$

$$\frac{dB_r}{dt} = a_r P_g - T_{ra} - R_{rt} - S_r \quad (14)$$

$$\frac{dB_{ad}}{dt} = S_a - L \quad (15)$$

where P_g (g DM d^{-1}) is the daily gross dry matter fixed through photosynthesis; a_r represents the dry matter allocation coefficient from aboveground parts to root tissues; T_{ra} (g DM d^{-1}) represents the carbohydrates transported from the roots to the living aboveground tissues; R_{at} (g DM d^{-1}) and R_{rt} (g DM d^{-1}) are total respiration from aboveground and root tissues, respectively; S_a (g DM d^{-1}) and S_r (g DM d^{-1}) represent the senescence rates of the living shoots and the roots, respectively, due to senescence; and L (g DM d^{-1}) is the litter fall, which is affected by the amount of precipitation.

Photosynthesis. Photosynthesis, the source of carbohydrates for the whole plant, is expressed as

$$P_g = R_a \varepsilon_c \varepsilon_l \varepsilon_e f_1(S) f_2(T_{air}) \quad (16)$$

where ε_c is the ratio of photosynthetically active radiation and extraterrestrial radiation; ε_l represents the efficiency of radiation absorption by green leaves; and ε_e is the energy efficiency. Functions f_1 and f_2 account for the stress incurred by soil moisture deficit and temperature, respectively.

$$\varepsilon_l = [1 - e^{(-k_l LAI_t)}\frac{LAI_g}{LAI_t}] \quad (17)$$

where k_l is an empiric constant; LAI_t is the total leaf area, consisting of green and dead leaves; and LAI_g represents the green leaf area.

$$LAI_g = C_g B_g \quad (18)$$

$$LAI_d = C_d B_d \quad (19)$$

$$LAI_t = LAI_g + LAI_d \quad (20)$$

where LAI_d is the dead leaf area, and c_g and c_d are empirical coefficients for living and dead biomass, respectively.

The effect of water stress on photosynthesis is estimated using the "static" water stress equation (Yetemen et al., 2015; Zhou et al., 2013) as a function of soil moisture condition and time.

$$f_1(S) = \begin{cases} 1, & S^* < S < 1 \\ 1 - \left[\frac{S^* - S}{S^* - S}\right]^{P_s}, & S_w < S \le S^* \\ 0, & 0 < S \le S_w \end{cases} \quad (21)$$

where, P_s is an empiric parameter referring to Yetemen et al. (2015).

Air temperature (T_{air}, °C) affects photosynthesis through the moderating activity of enzymes, and those effects are expressed as a piecewise function.

$$f_2(T_{air}) = \begin{cases} 1, & T_{opt} < T_{air} \\ 1 - \frac{T_{opt} - T_a}{T_{opt} - T_{min}}, & T_{min} \le T_{air} \le T_{opt} \\ 0, & T_{air} < T_{min} \end{cases} \quad (22)$$

where T_{min} and T_{opt} are the minimum and optimum temperatures, respectively, for photosynthesis.

Allocation. Dry matter allocation patterns are imperative for simulating the spatial patterns and temporal dynamics of plant biomass in terrestrial ecosystems. Herein, optimal partitioning theory (i.e., to maintain the homeostasis of the different nutrients or materials necessary for vegetation growth, biomass is allocated in priority to the construction of the organs responsible for capturing the most limiting resource) is adopted in the model. The allocation coefficient (a_r) is used to regulate the fraction of available carbohydrates allocated to aboveground and belowground parts. It is hypothesized that a balance must be maintained between shoots and roots such that the amount of aboveground phytomass does not exceed what the present root biomass can support (Nouvellon et al., 2000). This balance is described as:

$$B_{ax} = r_x B_{ag} - B_r \quad (23)$$

where r_x is the root-to-shoot ratio below which translocation occurs. If $B_{ax} > 0$, biomass is transported from the shoots to the roots. Otherwise, there is no biomass allocation. T_{ar} is calculated so that the root-to-shoot ratio is fixed to r_x at a daily time step:

$$r_x = \frac{B_r + T_{ar}}{B_{ag} - T_{ar}} \quad (24)$$

$$T_{ar} = \frac{B_{ax}}{1 + r_x} \quad (25)$$

$$a_r = \begin{cases} 1, & T_{ar} > P_g \\ \frac{T_{ar}}{P_g}, & T_{ar} \le P_g \end{cases} \quad (26)$$

However, a_r is given a value of 0.71 when the shoot senescence rate exceeds 0.012 (Nouvellon et al., 2000).

Root-to-shoot translocation. During early-season regrowth, or later in the season under some circumstances (for example, grazing has removed a critical amount of green biomass), carbohydrates will be transported from roots to shoots (T_{ra}). It is assumed that this translocation has occurred when (1) the 10-day average soil temperature is higher than 12.5 °C; (2) the average 5-day soil water potential is higher than -1.2 MPa; and (3) $B_r > r_x B_{ag}$. If all three conditions are met, then:

$$T_{ra} = t_r B_r \quad (27)$$

where t_r is the proportion of dry matter of the roots translocated to the shoots (=0.005 at 25 °C). It is assumed that translocation is a function of temperature, with a Q_{10}=3 (herein, Q_{10} describes the change in respiration with temperature rises 10 °C, for example, the Q_{10} modeled to be 3 means the

respiration triples per 10 ℃ rise in temperature (Hans Lambers, 2019)).

Respiration. For aboveground and root tissues, the rate of respiration is divided into two components: maintenance respiration and growth respiration. For the whole plant, total respiration (R_t) is the sum of aboveground respiration (R_{at}) and root respiration (R_{rt}).

$$R_{at} = m_a f_3(T_{air}) B_{ag} + g_a[(1 - a_r)P_g + T_{ra}] \tag{28}$$

$$R_{rt} = m_r f_3(T_{air}) B_r + g_r(a_r P_g) \tag{29}$$

where m_a and m_r represent the maintenance respiration rates for aboveground and root tissues, respectively; and g_a and g_r are the growth respiration rates for aboveground and root components, respectively. Function $f_3(T_{air})$ accounts for the effect of temperature on maintenance respiration rate with Q_{10}=2.

(5) Landform evolution

The topographic changes induced by the fluvial erosion and diffusive processes are simulated through the mass-transport continuity equation (Saco et al., 2007).

$$\frac{\partial z}{\partial t} = U - \frac{\nabla \cdot q_s}{\rho_s(1 - \eta_p)} - \nabla \cdot q_d \tag{30}$$

$$q_s = \beta_1 q^{m_1} S_p^{n_1} \tag{31}$$

$$q_d = D S_p \tag{32}$$

where z (m) is the topographic elevation; U (m d^{-1}) is the rate of tectonic uplift, which is ignored over a short time period; $\nabla \cdot$is the divergence operator; q_s (kg $d^{-1}m^{-1}$) is the fluvial sediment transport per unit width; q_d (m^3 d^{-1} m^{-1}) is the diffusive mass transport per unit width; ρ_s (kg m^{-3}) is the density of the sediment; n_p is the porosity of the sediment, (bold italics indicate vector quantities); S_P is the topographic slope; and D (m^3 d^{-1} m^{-1}) is the diffusion coefficient, to simulate diffusive transport processes (e.g., rainfall splash, soil creep).

Field observations and modeling studies of rainfall splash erosion or rill erosion in arable land have reported a strong nexus between rainfall erosivity and rainfall intensity (Carollo et al., 2018; Mermut et al., 1997); however, this impact of rainfall intensity on rainfall splash erosion was not included in the work of (Saco et al., 2007). In USFs, as PVs harvest rainfall and cause a concentrated downpour, the kinetic energy of the flow that drains from the panels was found to be greater than that of the rainfall alone (Cook Lauren and McCuen Richard, 2013), resulting in an enhancement of rain splash erosion along the drip lines. Therefore, it could be problematic to assess the impact of USFs on landscape erosion without considering changes of rainfall intensity (or the kinetic energy of water flowing out from edge of the PVs). Consequently, two modified diffusion coefficients, D_b and D_{PV}, for natural conditions and the land below PVs, respectively, are introduced into the SOFAR model, and calculated as an exponential function of rainfall according to results in Carollo et al. (2018):

$$D_b = \begin{cases} D_{bmin}, & P < P_{min} \\ D_{bmax} \cdot \left[1 - exp\left(\frac{P_{max} - P}{P_{max} - P_{min}} - 1\right)\right], & P_{min} \le P \le P_{max} \\ D_{max}, & P > P_{max} \end{cases} \tag{33}$$

$$D_{PV} = \begin{cases} D_{bmin}, & I_{PV} < P_{min} \\ [D_{bmax}K_{PV}A_r + D_{bmax}(1-A_r)] \cdot \\ \left[1 - exp\left(\frac{P_{max} - I_{PVs}}{P_{max} - P_{min}} - 1\right)\right], & P_{min} \le P \le P_{max} \\ D_{bmax}K_{PV}A_r + D_{bmax}(1-A_r), & I_{PV} > P_{max} \end{cases} \quad (34)$$

where P_{max}, 52.7 mm d^{-1}, is the observed daily maximum precipitation from 1980 to 2017 at the Wuzhong site; and P_{min} (mm d^{-1}) is a threshold, and rainfall splash erosion does not occur when the daily precipitation falls below this threshold, because of canopy interception (Laio et al., 2001). However, the minimum diffusion coefficient, D_{bmin}, is not equal to zero when precipitation is lower than P_{min}, because other diffusive erosion processes still occur. D_{bmax} is the maximum diffusive erosion rate. The weighed coefficient (1/6 in Eq. 9), is the ratio of the area of drip lines to shading area, which was used to calculate the weighed diffusion coefficient for the grid of installed PVs. The widespread method used to estimate kinetic energy of rainfall (K_e, in/h) described in (Wischmeier and Smith, 1978), is given by Eq. 36. According to Eq. 7 and Eq. 8, the amount of harvested rainfall by PVs is about five times that of natural rainfall, while the area of the drip line (A_r) is only one-six of the shading area below PVs (i.e., the projection area of PVs on the ground) (Figure 2b). Accordingly, the value of the kinetic energy parameter (K_{pv}), which was adopted to represent the changes of kinetic energy, was calculated from these three equations and is equal to 5.9.

$$K_e = 916 + 330log_{10}P \quad (35)$$

$$\beta_1 = \begin{cases} \beta_b(1-V_t)(1-\beta_v BV_t), & \beta_v B < 1 - \beta_{min}/\beta_b \\ \beta_{min}, & \beta_v B \ge 1 - \beta_{min}/\beta_b \end{cases} \quad (36)$$

where β_b is the maximum erodibility for bare soil, which is assumed to decrease linearly with increasing biomass density at a rate given by β_v to a minimum value given by β_{min}; and V_t (m^2 m^{-2}) is the vegetation coverage (Eq. 5).

2.3.2 The HC Index

Hydrological connectivity (HC) describes the internal physical linkages between runoff generation in the upper parts of a catchment and the water received through the fluvial system (Hooke, 2003; Van Nieuwenhuyse, 2012). Although the term HC is also used for subsurface flow (Buttle et al., 2004), we only consider Hortonian overland flow in this work, as it is the main runoff-generating mechanism in arid and semi-arid environments (Bryan and Yair, 1982). Since this study is concerned more with erosion behaviors than with other hydrological processes following the installation of USFs, we use a topography-based index of connectivity (*IC*) to understand hydrologic relationships among different parts of the catchment, and quantify the potential connections between hillslopes and features that act as targets or storage areas (sinks) for transported sediment. The index is defined as the ratio of the upslope connectivity (D_{up}) to the downslope connectivity (D_{dn}) (Borselli et al., 2008; Cavalli et al., 2013) , and higher *IC* value means a higher hydrologic connectivity:

$$IC_k = log_{10}\left(\frac{D_{up,k}}{D_{dn,k}}\right) = log_{10}\left(\frac{\overline{W_k} \cdot \overline{S_k}\sqrt{A_k}}{\sum d_i/(W_i \cdot S_i)}\right) \quad (37)$$

where W is the average weighting factor of the upslope contributing area (dimensionless), S is the average slope gradient of the upslope contributing area ($m \cdot m^{-1}$), A is the upslope contributing area

(m^2), d_i is the length of the i_{th} cell along the downslope path (m), W_i is the weight of the i_{th} cell (dimensionless, W_i ranges from 0 to 1), and S_i is the slope gradient of the i_{th} cell ($m \cdot m^{-1}$). More details of the methods used to calculate the upslope and downslope connectivity can be found in the literature (Cavalli et al., 2013).The DEM and raster maps of weighting factors with resolutions of 3 × 3 m were applied as the main input data for calculating *IC*. Further, by coupling with the indexes of HC, the SOFAR was used to simulate runoff for two conditions: pre- and post-development.

2.4 Parameterization and Scenario Setting

Before calibrating the parameters of the model, the most common parameter ranges were determined based on lab results, field survey results, and the related literature (Laio et al., 2001; Nouvellon et al., 2000). Eight months of field observations were divided into calibration period and validation period: i.e., observed volumetric water content (VWC) from 04/27/2021 to 09/07/2021 and collected vegetation samples in July 2021, were used to estimate parameters through the genetic algorithm (GE) by varying local soil and vegetation parameters within physically plausible ranges at the site, and field VWC from 09/10/2021 to 11/19/2021 were used to validate the simulation results of the SOFAR model. The estimated set of parameter values that could lead to a best fit of the modelled soil moisture behaviour with the measured data was used to run the scenario analysis. GE is a randomized search algorithm based on natural selection and genetic mechanisms in biology, which was employed to estimate the values of parameters based on observation results, with the Nash–Sutcliffe efficiency coefficient (NSE) as the fitness function (Appendix B). GE searches among a population of offered parameters, and works with a coding of the parameter set using probabilistic transition rules (Cheng et al., 2006). In this study, six settings were defined before running GE, including number of variables, population size, parent number, mutation rate, maximal generation, and minimal fitness value. Because the installation of runoff plots was not allowed at the Hongsibu site, the values of erosion parameters were the adopted empirical constants, as referred to in (Saco et al., 2007).

To estimate the effects of climate and terrain in controlling the effects of USFs on hydrological connectivity and soil erosion (Cook and McCuen, 2013), nine scenarios were designed by altering the mean annual precipitation amount, the frequency of precipitation events, and the ground slope (Table 1). Scenario 1 (S1) is the baseline scenario for comparison, in which the local climatic variables and landscape of the Hongsibu site were used to assess soil erosion following the installation of the solar farm. Because USFs are widely distributed across the climate gradient (150-800 mm yr^{-1}) of the Chinese Loess Plateau (van Hateren et al., 2022), Scenarios S2 and S3 were designed to represent the cases where USFs were built at other sites with similar thick loess soil on the plateau (Zhu et al., 2018), but where annual precipitation is two-fold and three-fold that of the Hongsibu site, respectively. Additional numerical scenarios (S4-S6) with increased rainfall variability (or decreased rainfall frequency, but where the amounts of annual precipitation were set to be the same as scenarios S1-S3, Figure S2), were investigated, to highlight the impacts of varied rainfall patterns on the hydrological behaviors in USFs in the context of climate change (Quijano-Baron et al., 2022).

Since terrain features (including slope, aspect, elevation, etc.) have been confirmed as among the

major potential factors in controlling the hydrological behavior of any region (Baartman et al., 2013; Cavalli et al., 2013), we also included terrain variables in our scenario analyses. However, because PV arrangements are dominantly determined by aspect, for siting USFs in hilly environments (i.e., if the terrain aspect changed, PV arrangements would be changed considerably), we did not consider the aspect of terrain in these analyses. The influence of terrain in this study was evaluated via the scenarios 7-9 (S7-S9), in which a 20% steeper terrain produced by stretching the DEM of the Hongsibu site was added to the scenarios 1-3 (S1-S3). Through this setting, about 1% of the PVs are distributed within the areas where slopes are higher than 20 degrees, which is the recommended slope limit for solar farm siting (Yang et al., 2019). To analyze the impact of catchment morphology, simulation results from the scenarios were also compared among the three delineated sub-catchments (T1-T3, Figure 1b, Table S2) at the Hongsibu site. In order to isolate the effects of USFs from original treatments, each scenario simulation was carried out twice—without PVs and with PVs. When the scenario with PVs was calculated, the 50-year period of evaluation was divided into three stages: pre-construction (8 years), construction (2 years) and operation (40 years), so that the influences of PVs on hydrological behaviors in USFs can be further highlighted through testing the differences between different stages.

3 Results

3.1 Model Performance and Parameter calibration

The estimated values for the model parameters are shown in Table 3. The simulation results of soil moisture driven by the observed daily meteorological variables at the Hongsibu site were tested against field observations. The model performed generally well at different positions, and captured the magnitudes of soil moisture responses to rainfall pulses and persistent evapotranspiration loss (NSE = 0.44~0.78) (Figure 3). However, a slight overestimation was still observed in the VWC (i.e., soil moisture corresponding to rainfall events). This discrepancy may be attributed to the simplified roof model and soil profile (i.e., the irregular flow of water above the PVs is simplified to a homogeneous downward flow), which caused the overestimated available water for soil and plants at the Front.

3.2 Effects of Solar Farm Construction on Soil Erosion

As shown in Figure 4 and Table S1, the human activities involved in the USF construction (e.g., removing vegetation) induced an average enhancement of 0.002 m to 0.009 m in accumulative soil erosion at the Hongsibu site. Compared to the cases without installation of a USF, PVs incurred averages of 66.48% (~0.005 m), 34.86% (~0.008 m), and 31.16% (~0.008 m) increase in soil erosion for scenarios with different annual precipitation amounts (S1-S3), respectively (Figures 4 and S3). Under the scenarios with higher rainfall variability (S4-S6), the soil erosion in the USF increased by up to 80.37% (0.006 m), 33.39% (0.009 m), and 30.12% (0.009 m), respectively (Figure 4b). However, soil erosion in the USF only slightly increased by 25.23% (0.002 m), 22.45% (0.007 m), and 18.07% (0.006 m), respectively, when relief amplitude increased by 20% (Scenarios S7 to S9,

Figure 4c). Furthermore, as shown in the map of soil erosion occurring over the whole site (Figure S4), a more serious erosion was clearly observed in the installation zones of the PVs, followed by the areas close to the riverway.

3.3 Effects of Solar Farm Operation on Soil Erosion

During the 40-year operating period of the USF, the deployed PVs incurred an average of 107.05% (0.138 m) deeper soil erosion compared with the corresponding cases without PVs (S1). Similar increases in soil erosion (42.92% to 116.40%) were also found in other simulation scenarios (S2-S9, Figure 4 and Table S2). Generally, our predicted results indicate that: (1) the cumulative soil erosion considerably increased with the mean annual amount of precipitation in cases both with and without PV deployment (Figure 4); (2) soil erosion showed higher sensitivity to rainfall variability than to either annual precipitation amount or terrain relief amplitude (Figure 5). The increase in soil erosion was most significant in Scenario S4 (116.4%), and least significant in Scenario S9 (42.92%). Among the scenarios of modified climate (S1-S6), increased annual precipitation (S1-S3) had more intense effects on soil erosion (Figure 5). The spatial pattern of soil erosion (Figure S6) indicates that soil erosion in areas away from the PVs had little difference from those of cases without PVs, and the most significant soil erosion was concentrated in the installation zones of PVs and in areas close to the riverway.

3.4 Linking Hydrologic Connectivity to Soil Erosion in a Solar Farm

As shown in Figure 6, the USF noticeably enhanced surface runoff, which is the primary driver of soil erosion, as is typically the case in the Loess Plateau. Specifically, during the installation period, construction activity of the USF incurred a 14.15% - 82.21% increase of mean annual runoff, compared with natural conditions; and during the long-term deployment of a USF, mean annual runoff could be approximately fifteen to forty times higher than that of natural conditions (Table S3). We tested the hydrologic connectivity before and after PV installment in the USF. Our results indicated that the effect of the PVs on local HC was limited in the USF (Figure 6). The construction activity of the USF increased by averages of 0.005, 0.026, and 0.12 in HC for the scenarios of increased annual precipitation (S1-S3), increased rainfall variability (S4-S6), and increased relief amplitude (S7-S9), respectively, whereas, after the forty years operation of the USF, HC increased by up to 0.232, 0.149, and 0.314 for each group of scenarios, respectively.

We further compared the HC patterns of the delineated sub-catchments in the USF (T1-T3). Overall, the areas close to the fluvial or basin outlets were usually associated with higher hydrologic connectivity (Figure 7). The spatial-temporal patterns of background HC differed between the three sub-catchments, and the background HC for the sub-catchments T1, T2, and T3 were -2.05, -1.97, and -2.16, respectively. The HC showed a continuous increase trend for both construction and operation periods, whereas the USF showed a difference of HC from that of natural conditions. For example, for the construction period, the HC of sub-basins T1 through T3 increased by 0.4%, 0.3%, and 0.7%, respectively, while when the USF continuedly operated for 40 years, the HC increased by 10.4%, 10.1%, and 6.9% for sub-basins T1 through T3, respectively. Furthermore, our results

presented that the landscapes with higher hydrologic connectivity (i.e., higher IC value) were more likely to be exposed to the risks of soil erosion (Table S4). For example, the average HC (soil erosion) values of sub-basins T1 and T2 were 4.4% (40%) and 8.4% (15%) higher, respectively, than that of sub-basin T3.

4 Discussion

4.1 Does a solar farm increase soil erosion by increasing HC?

In recent years, USFs with the potential to incur an increase in runoff or flood peak time have been reported Nair et al. (2022). For example, Cook and McCuen (2013) reported that when compared to areas without a solar farm, photovoltaic panels incurred 7% and 73% of the increase in storm runoff and peak discharge, respectively. Our predicted results also confirm that the USFs incurred a 14% ~ 4046% increase in annual runoff. For soil erosion in the USF, previous researches have reported that PVs might be favorable for co-located vegetation (Adeh et al., 2018; Barron-Gafford et al., 2019; Cook, 2011; Marrou et al., 2013), which in turn might mitigate the erosion caused by concentrated flows caused by PVs. This conjecture, however, was not supported by our results, which indicate that soil erosion increases by 58% ~ 88.25%. Our modeling results indicate that this positive effect cannot fully offset the negative ones from PVs, especially when solar farms are built in areas characterized by high HC, annual precipitation is higher, or extreme precipitation events are frequent (Figure 4).

Soil erosion rate is a function of rain splash and runoff (Battany and Grismer, 2000). For a USF, rain splash is the dominant factor causing erosion because PVs redistribute rainfall and amplify its intensity along the drip lines (~ five times higher than natural rainfall intensity at the Hongsibu site). However, rain splash erosion does not redistribute large amounts of soil; rather, it serves to detach soil particles for transport by runoff (Battany and Grismer, 2000). Our results indicated that runoff explains 78% ~ 95% of the changes of soil erosion in a solar farm (Figure 8 a and b). However, we argue that runoff is not the only dominative factor for soil erosion when up to forty years of deployment of a USF is considered. As shown in the Figure 6, while the USF changed HC in the site, the changes in HC could also have affected soil erosion through changing the capacity of the transporting sediment, a result supported by the positive relationship between HC and soil erosion (Figure 8 c and d).

Based on predicted results in this study, we conceptualized the mechanism of a USF's effect on soil erosion as a positive feedback between runoff and HC: i.e., an increase in runoff incurs serious soil erosion and necessitates more developed river networks, and such development represents higher HC and stronger sediment transport capacity, as well as more concentrated runoff. As a result, higher HC can further increase soil erosion due to changes in junction paths. For example, PV panels act as an imperious cover, and thus rainfall is concentrated along the downslope edge of the panels, incurring increased runoff, as well as rain splash erosion risks (Holland, 2021; Smith et al., 2011). Raindrop impacts are responsible for particle detachment and the creation of micro topography (Josserand and Zaleski, 2003), and this local erosion in turn might potentially create additional pathways for runoff and increase HC, thus furthering soil degradation processes at larger scales (Elamri et al., 2018).

4.2 Does higher background HC aggravate the effects of USFs?

Besides causing local erosion along the edge of the panel via enhanced kinetic energy (Cook and McCuen, 2013), the significantly concentrated rainwater on the ground surface near PV panels seems more likely to generate Hortonian overland flow and floods on the slopes of hilly ground, and the eroded soil under PV panels is also more likely to reach a transport system in hilly environments, and subsequently to result in considerable off-site sediment movement in USFs (Hernandez et al., 2014). For example, under the same precipitation conditions, we found that the landscapes with higher HC (i.e., higher IC value) were more likely to be exposed to the danger of soil erosion (Figure 4 and Figure 6). Further, the more severe soil erosion in solar farms with higher relief amplitudes could be explained at least partly by the relatively higher HC in steeper terrain. From the modeling results of this work, it is also interesting to find that even USFs with similar relief amplitudes could result in very different effects on the soil erosion processes, as more dramatic changes and higher HC were usually detected in areas where a solar farm was sited (Figures S4 and S6). This phenomenon might be related to the fact that higher HC often leads to shorter runoff time and larger runoff kinetic energy (Poesen et al., 2003), and thus is more likely to build connections between PV-caused erosion at local scales and sediment transfers at larger scales in USFs with higher background HC (Holland, 2021; Smith et al., 2011). Similarly, increasing vegetation cover could lower the HC in USFs, and thus significantly reduce the risk of erosion. The basic logic behind these measures is that they protect the surface by restricting the movement of sediment and increase the hydraulic conductivity of the soil, resulting in greater throughflow and less overland flow, thereby reducing HC and erosion (Greenville, 2022; Phalane, 2021).

4.3 Implications for Risk Control of USFs in Hilly Environments

USFs offer an opportunity to deliver ecosystem co-benefits, but their development and operation may also incur detrimental consequences to ecosystems (Randle-Boggis et al., 2020). Regarding the negative impact of USFs, some of the top concerns from governments and local communities are the risks of stormwater runoff and erosion (Brick, 2019; Chiabrando et al., 2009). Depending on their scale, PVs could bring risks to either local or surrounding environments by the installation and operation of the USFs. USFs on hilly terrain, especially, tend to produce even more stormwater erosion and sediment risks to both local and surrounding regions (Awasthi et al., 2022). These concomitant pressures on the ambient environment obviate the need to consider standardized and science-based regulations (for example, suitable USF designs and storm-water management facilities (Phalane, 2021)) to prevent potential impacts from USF installation and development (Lee, 2019). From the perspective of hydrological connectivity, controlling the risks of stormwater erosion in USFs can also be achieved through measures that reduce the HC: e.g., a gutter system can be installed to capture all the stormwater falling on the PV panels and redirect it into a stormwater attenuation tank or infiltration soak-away (Phalane, 2021); on-site flood control structures (e.g., earthen berms, diversion ditches, and stormwater conveyance channels) can be constructed along the contour lines and across slopes for the purpose of intercepting surface runoff and diverting it to suitable outlets (Brick, 2019; Doorga et al., 2022; Murphy-Mariscal et al., 2018); buffer strips,

558 detention basins or swales can even be built at the downgradient end of the application site to reduce
559 the peak run-off rate or intercept extreme flows that may already be running offsite (Farm and Street,
560 2021; Greenville, 2022; Phalane, 2021).

561 Furthermore, to minimize the impact on ecohydrological processes in landscapes, USFs should be
562 installed at locations with minimal flood risk, to limit damage from soil erosion near the facility's
563 infrastructure (Belding et al., 2020): e.g., avoiding steeply sloped sites will reduce the potential for
564 erosion, sedimentation, and runoff, and thus protect the local ecological functions and avoid
565 tremendous soil erosion (Wiseman et al., 2022). Furthermore, drainage systems have often been
566 overlooked at location sittings, and should be better investigated (Phalane, 2021). According to Lee
567 (2019) and Shobe (2022), the angle and height of the photovoltaic arrays might also affect the
568 amount of runoff and kinetic energy. Correspondingly, the optimal angle and height design of USFs
569 in hilly environments should be taken into account the erosion issues arising from concentrated flows
570 in drip-lines or the direct mechanical effects of droplet impacts (Elamri et al., 2018; Josserand and
571 Zaleski, 2003), in addition to the principle of maximizing the solar energy capture (Gumiere et al.,
572 2009; Knapen et al., 2007). Where possible, herbaceous vegetation recruitment or re-establishment
573 under the PVs is imperative, to provide soil stability and minimize soil erosion (Greenville, 2022). A
574 combination of a USF planting process and allowing the naturally occurring vegetation to replenish
575 itself with time can accomplish this goal (Cook and McCuen, 2013). When evaluating the potential
576 to co-locate vegetation with solar infrastructure, the redistribution of soil moisture by PVs—which
577 could potentially be used in concert with planting strategies to maximize plant growth or minimize
578 soil erosion—should also be considered (Choi et al., 2020). Furthermore, there is always a need for
579 more field research on less ideal sites such as those with steeper slopes, greater gully density, and
580 more loessy soils (Yavari et al., 2022). It is also recommended that erosion and silt management be
581 considered carefully and monitored regularly in these hilly environments (Dhar et al., 2020; Phalane,
582 2021).

583 ## 5 Conclusions

584 The potential effects of USFs on soil erosion in hilly environments were investigated in this work
585 from the perspective of hydrological connectivity, using the SOFAR model. Our results show that
586 land use changes in the construction of solar farms (e.g., vegetation removal) incur a significant
587 increase in soil erosion rates; accumulative soil erosion increased by 22.45% ~ 66.48% for nine
588 simulation scenarios, during the installation period. During the 40-year deployment period of the
589 USFs, photovoltaic panels (PVs) incurred an average of 0.138 m deeper erosion compared with the
590 background rate without PVs; a wetter climate will obviously incur higher erosion. The relief
591 amplitude of the terrain and precipitation frequency are also confirmed as important controlling
592 factors for soil erosion. We conclude that USFs can increase soil erosion, mainly by increasing local
593 HC and runoff, and higher background HC in turn can further aggravate the effects of USFs on soil
594 erosion. Accordingly, through suitable USF designs and storm-water management that can
595 potentially reduce the HC or at least prevent any increases in it, erosion-related risks caused by
596 photovoltaic panels (PVs) within and around USFs can be considerably lowered. The outcomes from
597 this study provide useful guidance for assessing the potential hydrologic effects of USF installation
598 and operation in hilly environments—important information for those who plan, design, and deploy

USF projects, especially in the context of climate change and increasing land scarcity.

Appendix A

The components of the solar irradiance incident on an inclined photovoltaic panel (PV) are: beam radiation coming directly from the sun, diffuse radiation from the entire hemisphere, and ground-reflected radiation. As reported in the literature, each of these components of solar irradiance incident on a photovoltaic panel is determined by calculating solar incidence angle (i), solar elevation angle (h_c) (Diez et al., 2021; Passias and Källbäck, 1984), solar declination (δ), and hour angle (ω). Aspect-controlled radiation has been recognized as a vital driver responsible for the co-evolution of vegetation, soil, and landscape (Kumari et al., 2020; Yetemen et al., 2015; Zhou et al., 2013), which is also considered in this study, in order to avoid additional biases.

The daily extraterrestrial radiation (I_0, w m^{-2}) is estimated using the following equation:

$$I_0 = 1353\left[1 + 0.034cos\left(\frac{2\pi n}{365}\right)\right]\frac{sin(h_c)}{\sin(h_c) + \mathrm{C}} \tag{A1}$$

where parameter C, relating to atmospheric transparency, is an empirical coefficient, and solar elevation angle and solar incidence angle are estimated by Eq. A2 and Eq. A3, respectively.

$$sin(h_c) = sin(\varphi)sin(\delta) + cos(\varphi)cos(\delta)cos(\omega) \tag{38}$$

$$\begin{aligned} cos(i) = {} & sin(\delta)[sin(\varphi)cos(\beta) - cos(\varphi)sin(\beta)cos(\gamma)] \\ & + cos(\delta)cos(\omega)[cos(\varphi)cos(\beta) + sin(\varphi)sin(\beta)cos(\gamma)] \\ & + cos(\delta)sin(\beta)sin(\gamma)sin(\omega) \end{aligned} \tag{A3}$$

where parameters φ, β, and γ represent the latitude of the site, the inclination angle of the PV, and the azimuth angle of the PV (or aspect of each grid), respectively. The solar declination (δ) and the hour angle (ω) are given by

$$\delta = 23.45sin\left(360\frac{284 + N}{365}\right) \tag{A4}$$

$$\omega = (\tau - 12)15^{\circ} \tag{A5}$$

where N is the day of the year, and the solar time τ is given by

$$\tau = T + \frac{E - 4\left(12 - L_{log}\right)}{60} \tag{A6}$$

where T (h) is Beijing time, L_{log} is the local longitude, and E (min)—the corrected time difference attributable to the change in the speed of the earth's motion around the sun (Gualla, 2015)—is given by

$$E = 9.87sin(2B) - 7.53cos(B) - 1.5sin(B) \tag{A7}$$

$$B = \frac{360(n - 81)}{365} \tag{A8}$$

The total available solar radiation on an inclined PV is the sum of beam radiation, diffuse radiation, and ground-reflected radiation (Diez et al., 2021).

$$I_{PV} = I_{b\beta} + I_{d\beta} + I_r \tag{A9}$$

Beam radiation (MJ m^{-2}) can be estimated based on extraterrestrial radiation (I_0, W m^{-2}). Beam

radiation incident on a horizontal surface and on an inclined photovoltaic panel are given by Eq. 17 and Eq. 18, respectively.

$$I_{bH} = I_0 P^m sin(h_c) \tag{A10}$$

$$I_{b\beta} = I_0 P^m cos(i) \tag{A11}$$

where P—atmospheric transparency—is a constant. The constant m—atmospheric quality—is a function of solar elevation angle ($m = 1/sin(h_c)$).

Diffuse radiation from the entire hemisphere incident on a horizontal surface is estimated as

$$I_{dH} = \frac{1}{2} I_{bH} \frac{1 - P^m}{1 - 1.4\ln(P)} F = 1 - \left(\frac{I_{dH}}{I_0}\right)^2 \tag{A12}$$

Diffuse radiation from the sky incident on an inclined PV ($I_{d\beta}$), estimated from I_{dH}, is given by the Klucher model of anisotropic distribution for all sky types (Klucher, 1979).

$$I_{d\beta} = I_{dH}\left(1 + cos(\beta)\right)\left[1 + Fsin^3(\frac{\beta}{2})\right][1 + Fcos^2(i)cos^3(h_c)] \tag{A13}$$

$$F = 1 - \left(\frac{I_{dH}}{I_0}\right)^2 \tag{A14}$$

The radiation reflected by the ground surface, incident on an inclined PV under anisotropic reflection assumption (Diez et al., 2021), is presented thus:

$$I_r = \frac{1}{2}\alpha(I_{bH} + I_{dH})[1 - cos(\beta)]\left[1 + sin^2\left(\frac{\pi}{4} - \frac{h_c}{2}\right)\right] \tag{A15}$$

where α is the ground albedo (i.e., the ratio of irradiation reflected from the ground to the irradiation incident on the ground).

Daily solar radiation values from 1980 to 2017 were not available; only daily sunshine duration (SSD) could be found. An alternative algorithm was therefore adopted to calculate the daily solar radiation. Daily solar radiation is equal to SSD multiplied by the daily average solar radiation, which is the average of all the per-hour solar radiation values projected by Eqs.A1 to A8. The model assumes that every growing season has the same average solar radiation at the daily scale, and this is produced on the basis of 12 hours of SSD, so that daily solar radiation can be calculated from SSD records. The total available solar radiation on the horizontal ground surface and on a PV can be calculated by

$$I_G = \frac{\sum_j^{12}\left(I_{bH,j} + I_{dH,j}\right)}{12} \tag{A16}$$

$$I_{PV} = \frac{\sum_j^{12}\left(I_{b\beta,j} + I_{d\beta,j} + I_{r,j}\right)}{12} \tag{A17}$$

In a large-scale solar farm where the panels are mounted in rows, there is a masking effect: i.e., the panels in all the rows except the first one experience a partial blocking of the hemispheric radiation, and thus there is a reduction in the amount of diffuse radiation they receive (Passias and Källbäck, 1984). Therefore, the total available radiation for the sheltered area is estimated as

$$I_s = I_{PV}(1 - \varepsilon - \alpha_{PV})\eta + I_{ds} \tag{A18}$$

where ε is the efficiency with which a PV transfers the solar radiation to electricity, α_{PV} is the albedo of the PV's surface, and η is the PV's re-radiation coefficient. I_{dS} is the available diffuse radiation of the sheltered area.

$$I_{ds} = I_{dH}\frac{\xi}{\pi} \tag{A19}$$

where ξ is shading angle of the PV, which is given by

$$\xi = \pi - \arctan\left(\frac{h}{W}\right) - \arctan\left(\frac{H}{Lcos(\beta) - W}\right) \tag{A20}$$

where h (m) and H (m) are the height of the front and rear edges of the PV, respectively; L (m) is the length of the PV; and W (m) is the distance from a point in the sheltered zone to the front edge of the PV.

Appendix B

The statistical index, Nash–Sutcliffe efficiency coefficient (NSE), was used for assessing the accuracy of the SOFAR model.

$$NSE = 1 - \frac{\sum_i^n \left(Q_0^i - Q_S^i\right)^2}{\sum_i^n \left(Q_0^i - \overline{Q_0}\right)^2} \tag{B1}$$

Where Q_0^i and Q_S^i are observation and simulation results of daily VWC (v/v), respectively, i is the number of days in the calibration period, and $\overline{Q_0}$ is the average of field observation of soil moisture content.

Annual rainfall variability was calculated as the ratio standard deviation (*Std*) of annual precipitation and annual average precipitation (*Mean*).

$$CV = Std/Mean \tag{B2}$$

Acknowledgements

This research was jointly supported by the National Natural Science Foundation of China (42171117 / 42177310), the Strategic Priority Research Program of the Chinese Academy of Sciences (XDA2003010102), and the 2232 International Fellowship for Outstanding Researchers Program of the Scientific and Technological Research Council of Turkey (118C329). The authors thank the editor (Dr. Peter Troch) and the anonymous reviewers for their valuable comments and suggestions.

Open Research

The daily meteorological observations (1980-2016) on which this article is based are available in Ren et al. (2021). The field observations of biomass, soil moisture dynamics and other microclimates used in this study are archiving, and will be available from the data-sharing website of Linze Station, Chinese Ecosystem Research Network (http://lzd.cern.ac.cn/meta/metaData). Code of the SOFAR model (solar farm model) used in this study will be available at https://github.com/LIUHOOOO/SOFAR-3.2.

Author contributions

H.L. and C.W. are the co-first authors and contributed equally to this work. H.L. provided insights and designed the study. H.L. and C.W. performed the analysis and drafted the manuscript with contribution from co-authors. Y.Y., W.Z., and O.Y. discussed, reviewed, and edited the manuscript.

Competing financial interests

The authors declare no competing interests.

References

Adeh E. H., Selker J. S., Higgins C. W., Villarini M. (2018). Remarkable agrivoltaic influence on soil moisture, micrometeorology and water-use efficiency. *PLoS ONE*, 13, https://dor.org/10.1371/journal.pone.0203256.

Armstrong A., Ostle N. J., Whitaker J. (2016). Solar park microclimate and vegetation management effects on grassland carbon cycling. *Environmental Research Letters*, 11, 074016. https://doi.org/10.1088/1748-9326/11/7/074016.

Awasthi A., Kallioğlu M. A., Sharma A., Mohan A., Chauhan R., Singh T. (2022). Solar collector tilt angle optimization for solar power plant setup-able sites at Western Himalaya and correlation formulation. *Journal of Thermal Analysis and Calorimetry*, 1-15. https://dor.org/10.1007/s10973-022-11345-0.

Baartman J. E. M., Masselink R., Keesstra S. D., Temme A. J. A. M. (2013). Linking landscape morphological complexity and sediment connectivity. *Earth Surface Processes and Landforms*, 38, 1457-1471. https://doi.org/10.1002/esp.3434.

Baartman J. E. M., Temme A. J. A. M., Saco P. M. (2018). The effect of landform variation on vegetation patterning and related sediment dynamics. *Earth Surface Processes and Landforms*, 43, 2121-2135. https://doi.org/10.1002/esp.4377.

Barron-Gafford G. A., Pavao-Zuckerman M. A., Minor R. L., Sutter L. F., Barnett-Moreno I., Blackett D. T., Thompson M., Dimond K., Gerlak A. K., Nabhan G. P. (2019). Agrivoltaics provide mutual benefits across the food–energy–water nexus in drylands. *Nature Sustainability*, 2, 848-855. https://dor.org/10.1038/s41893-019-0364-5.

Battany M. C., Grismer M. E. (2000). Rainfall runoff and erosion in Napa Valley vineyards: effects of slope, cover and surface roughness. *Hydrological Processes*, 14, 1289-1304. https://doi.org/10.1002/(SICI)1099-1085(200005)14:7<1289::AID-HYP43>3.0.CO;2-R.

Belding S., Walker H., Watson A. C.: National Renewable Energy Lab.(NREL), Golden, CO (United States), 2020.

Boix-Fayos C., de Vente J., Barberá G., Castillo V. (2007). The impact of land use changes and hydrological control works on hydrological connectivity and sediment yield at the catchment scale; proceedings of the European Geosciences Union General Assembly, Location: Vienna, Austria, F, 2007. Published.

Bolinger M., Seel J. Utility-Scale Solar: Empirical Trends in Project Technology, Cost, Performance, and PPA Pricing in the United States. 2018.

Bórawski P., Bełdycka-Bórawska A., Szymańska E. J., Jankowski K. J., Dubis B., Dunn J. W. (2019). Development of renewable energy sources market and biofuels in The European Union. *Journal of cleaner production*, 228, 467-484. https://dor.org/10.1016/j.jclepro.2019.04.242.

Borselli L., Cassi P., Torri D. (2008). Prolegomena to sediment and flow connectivity in the landscape: A GIS and field numerical assessment. *Catena*, 75, 268-277. https://doi.org/10.1016/j.catena.2008.07.006.

Bracken L. J., Croke J. (2007). The concept of hydrological connectivity and its contribution to understanding runoff-dominated geomorphic systems. *Hydrological Processes: An International Journal*, 21, 1749-1763. https://dor.org/10.1002/hyp.6313.

Brick R. (2019). Utility-Scale Solar Construction: Best Practices for Reducing Costs and Ensuring Environmental Compliance.

Bryan R., Yair A. (1982) Badland geomorphology and piping. Norwich: Geo Books.

Buttle J., Dillon P., Eerkes G. (2004). Hydrologic coupling of slopes, riparian zones and streams: an example from the Canadian Shield. *Journal of Hydrology*, 287, 161-177. https://dor.org/10.1016/j.jhydrol.2003.09.022.

Cabal C., De Deurwaerder H. P. T., Matesanz S. (2021). Field methods to study the spatial root density distribution of individual plants. *Plant and Soil*, 462, 25-43. https://doi.org/10.1007/s11104-021-04841-z.

Carollo F. G., Ferro V., Serio M. A. (2018). Predicting rainfall erosivity by momentum and kinetic energy in Mediterranean environment. *Journal of Hydrology*, 560, 173-183. https://doi.org/10.1016/j.jhydrol.2018.03.026.

718 Cavalli M., Trevisani S., Comiti F., Marchi L. (2013). Geomorphometric assessment of spatial sediment connectivity in small Alpine
719 catchments. *Geomorphology*, 188, 31-41. https://doi.org/10.1016/j.geomorph.2012.05.007.
720 Chen J., P. Brissette F., Leconte R., Caron A. (2012). A Versatile Weather Generator for Daily Precipitation and Temperature.
721 *Transactions of the ASABE*, 55, 895-906. https://doi.org/10.13031/2013.41522.
722 Cheng C.-T., Zhao M.-Y., Chau K. W., Wu X.-Y. (2006). Using genetic algorithm and TOPSIS for Xinanjiang model calibration with a
723 single procedure. *Journal of Hydrology*, 316, 129-140. https://doi.org/10.1016/j.jhydrol.2005.04.022.
724 Chiabrando R., Fabrizio E., Garnero G. (2009). The territorial and landscape impacts of photovoltaic systems: Definition of impacts
725 and assessment of the glare risk. *Renewable & Sustainable Energy Reviews*, 13, 2441-2451.
726 https://doi.org/10.1016/j.rser.2009.06.008.
727 Choi C. S., Cagle A. E., Macknick J., Bloom D. E., Caplan J. S., Ravi S. (2020). Effects of Revegetation on Soil Physical and
728 Chemical Properties in Solar Photovoltaic Infrastructure. *Frontiers in Environmental Science*, 8,
729 https://doi.org/10.3389/fenvs.2020.00140.
730 Cook Lauren M., McCuen Richard H. (2013). Hydrologic Response of Solar Farms. *Journal of Hydrologic Engineering*, 18, 536-541.
731 https://dor.org/10.1061/(ASCE)HE.1943-5584.0000530.
732 Cook L. M., McCuen R. H. (2013). Hydrologic response of solar farms. *Journal of Hydrologic Engineering*, 18, 536-541.
733 https://doi.org/10.1061/(ASCE)HE.1943-5584.0000530.
734 Cook P. (2011). Infrastructure, rural electrification and development. *Energy for Sustainable Development*, 15, 304-313.
735 https://dor.org/10.1016/j.esd.2011.07.008.
736 Dhar A., Naeth M. A., Jennings P. D., Gamal El-Din M. (2020). Perspectives on environmental impacts and a land reclamation strategy
737 for solar and wind energy systems. *Science of the Total Environment*, 718, 134602. https://dor.org/10.1016/j.scitotenv.2019.134602.
738 Dhonde M., Sahu K., Murty V. V. S. (2022). The application of solar-driven technologies for the sustainable development of
739 agriculture farming: a comprehensive review. *Reviews in Environmental Science and Bio/Technology*, 21, 139-167.
740 https://dor.org/10.1007/s11157-022-09611-6.
741 Diez F. J., Martínez-Rodríguez A., Navas-Gracia L. M., Chico-Santamarta L., Correa-Guimaraes A., Andara R. (2021). Estimation of
742 the Hourly Global Solar Irradiation on the Tilted and Oriented Plane of Photovoltaic Solar Panels Applied to Greenhouse
743 Production. *Agronomy*, 11, 495. https://doi.org/10.3390/agronomy11030495.
744 Doorga J., Rughooputh S., Boojhawon R. (Yeear) Geolocating Optimum Sites for Solar Farms. Geospatial Optimization of Solar
745 Energy. Springer. 35-52. https://dor.org/10.1007/978-3-030-95213-6_4.
746 Dunne T., Zhang W., Aubry B. F. (1991). Effects of Rainfall, Vegetation, and Microtopography on Infiltration and Runoff. *Water*
747 *Resources Research*, 27, 2271-2285. https://doi.org/10.1029/91WR01585.
748 E.Tanner K., A.Moore-O'Leary K., M.Parker I., M.Pavlik B., R.Hernandez R. (2020). Simulated solar panels create altered
749 microhabitats in desert landforms. *Ecosphere*, 11, e03089. https://doi.org/10.1002/ecs2.3089.
750 Edalat M. M. (2017). Remote sensing of the environmental impacts of utility-scale solar energy plants. *University of Nevada, Las*
751 *Vegas*.
752 Elamri Y., Cheviron B., Mange A., Dejean C., Liron F., Belaud G. (2018). Rain concentration and sheltering effect of solar panels on
753 cultivated plots. *Hydrology and Earth System Sciences*, 22, 1285-1298. https://doi.org/10.5194/hess-22-1285-2018.
754 Farm M., Street M. (2021). Tewkesbury borough council–development management.
755 Foerster S., Wilczok C., Brosinsky A., Segl K. (2014). Assessment of sediment connectivity from vegetation cover and topography
756 using remotely sensed data in a dryland catchment in the Spanish Pyrenees. *Journal of Soils and Sediments*, 14, 1982-2000.
757 https://doi.org/10.1007/s11368-014-0992-3.
758 Freeman M. C., Pringle C. M., Jackson C. R. (2007). Hydrologic connectivity and the contribution of stream headwaters to ecological
759 integrity at regional scales 1. *JAWRA Journal of the American Water Resources Association*, 43, 5-14.
760 https://dor.org/10.1111/j.1752-1688.2007.00002.x.
761 Greenville S. (2022). Draft environmental impact statement.

Gualla F. (2015). Sun position and PV panels : a model to determine the best orientation. *Lund University*,

Guan J., Wang Y., Sun Y., Wang S. (2020). Suitable period and change of tourism climate in Ningxia in the past 39 years. *Arid Land Geography*, 43, 339-348.

Gumiere S. J., Le Bissonnais Y., Raclot D. (2009). Soil resistance to interrill erosion: Model parameterization and sensitivity. *CATENA*, 77, 274-284. https://dor.org/10.1016/j.catena.2009.02.007.

Hans Lambers R. S. O. (Yeear) 2. Photosynthesis, Respiration, and Long-Distance Transport. Plant Physiological Ecology. Springer Cham. 127. https://doi.org/10.1007/978-3-030-29639-1.

Hernandez R. R., Easter S. B., Murphy-Mariscal M. L., Maestre F. T., Tavassoli M., Allen E. B., Barrows C. W., Belnap J., Ochoa-Hueso R., Ravi S. (2014). Environmental impacts of utility-scale solar energy. *Renewable & Sustainable Energy Reviews*, 29, 766-779. https://doi.org/10.1016/j.rser.2013.08.041.

Hernandez R. R., Hoffacker M. K., Murphy-Mariscal M. L., Wu G. C., Allen M. F. (2015). Solar energy development impacts on land cover change and protected areas. *Proceedings of the National Academy of Sciences of the United States of America*, 112, 13579-13584. https://doi.org/10.1073/pnas.1517656112.

Higgisson W., Higgisson B., Powell M., Driver P., Dyer F. (2020). Impacts of water resource development on hydrological connectivity of different floodplain habitats in a highly variable system. *River Research and Applications*, 36, 542-552. https://doi.org/10.1002/rra.3409.

Holland R. (2021). Development of a Solar Park Carbon Calculator (SPCC) to assist deployment decisions. *Lancaster University*.

Hooke J. (2003). Coarse sediment connectivity in river channel systems: a conceptual framework and methodology. *Geomorphology*, 56, 79-94. https://dor.org/10.1016/S0169-555X(03)00047-3.

Hu A., Levis S., Hu A., Levis S., Meehl Gerald A., Han W., Washington Warren M., Oleson Keith W., van Ruijven Bas J., He M., Strand Warren G. (2016). Impact of solar panels on global climate. *Nature Climate Change*, 6, 290-294. https://doi.org/10.1038/nclimate2843.

Istanbulluoglu E., Wang T., Wedin D. A. (2012). Evaluation of ecohydrologic model parsimony at local and regional scales in a semiarid grassland ecosystem. *Ecohydrology*, 5, 121-142. https://doi.org/10.1002/eco.211.

Jahanfar A., Drake J., Gharabaghi B., Sleep B. (2020). An experimental and modeling study of evapotranspiration from integrated green roof photovoltaic systems. *Ecological Engineering*, 152, 105767. https://doi.org/10.1016/j.ecoleng.2020.105767.

Jahanfar A., Drake J., Sleep B., Margolis L. (2019). Evaluating the shading effect of photovoltaic panels on green roof discharge reduction and plant growth. *Journal of Hydrology*, 568, 919-928. https://doi.org/10.1016/j.jhydrol.2018.11.019.

Josserand C., Zaleski S. (2003). Droplet splashing on a thin liquid film. *Physics of fluids*, 15, 1650-1657. https://dor.org/10.1063/1.1572815.

Klucher T. M. (1979). Evaluation of models to predict insolation on tilted surfaces. *Solar Energy*, 23, 111-114. https://doi.org/10.1016/0038-092X(79)90110-5.

Knapen A., Poesen J., Govers G., Gyssels G., Nachtergaele J. (2007). Resistance of soils to concentrated flow erosion: A review. *Earth-Science Reviews*, 80, 75-109. https://dor.org/10.1016/j.earscirev.2006.08.001.

Kompanizare M., Petrone R. M., Shafii M., Robinson D. T., Rooney R. C. (2018). Effect of climate change and mining on hydrological connectivity of surficial layers in the Athabasca Oil Sands Region. *Hydrological Processes*, 32, 3698-3716. https://doi.org/10.1002/hyp.13292.

Kruitwagen L., Story K. T., Friedrich J., Byers L., Skillman S., Hepburn C. (2021). A global inventory of photovoltaic solar energy generating units. *Nature*, 598, 604-610. https://doi.org/10.1038/s41586-021-03957-7.

Kumari N., Saco P. M., Rodriguez J. F., Johnstone S. A., Srivastava A., Chun K. P., Yetemen O. (2020). The Grass Is Not Always Greener on the Other Side: Seasonal Reversal of Vegetation Greenness in Aspect-Driven Semiarid Ecosystems. *Geophysical Research Letters*, 47, https://dor.org/10.1029/2020gl088918.

Laio F., Porporato A., Ridolfi L., Rodriguez-Iturbe I. (2001). Plants in water-controlled ecosystems: active role in hydrologic processes and response to water stress: II. Probabilistic soil moisture dynamics. *Advances in Water Resources*, 24, 707-723.

https://doi.org/10.1016/S0309-1708(01)00005-7.

Lee S. (2019). Erosion and Storm Water Runoff: sPower Solar Farm Project: Watershed Environmental Analysis.

Liu Y., Zhang R., Huang Z., Cheng Z., Lopezvicente M., Ma X., Wu G. (2019). Solar photovoltaic panels significantly promote vegetation recovery by modifying the soil surface microhabitats in an arid sandy ecosystem. *Land Degradation & Development*, 30, 2177-2186. https://doi.org/10.1002/ldr.3408.

Makaronidou M. (2020). Assessment on the Local Climate Effects of Solar Photovoltaic Parks. *Lancaster University*.

Marrou H., Guilioni L., Dufour L., Dupraz C., Wery J. (2013). Microclimate under agrivoltaic systems: Is crop growth rate affected in the partial shade of solar panels? *Agricultural and Forest Meteorology*, 177, 117-132. https://dor.org/10.1016/j.agrformet.2013.04.012.

Mermut A. R., Luk S. H., Römkens M. J. M., Poesen J. W. A. (1997). Soil loss by splash and wash during rainfall from two loess soils. *Geoderma*, 75, 203-214. https://doi.org/10.1016/S0016-7061(96)00091-2.

Murphy-Mariscal M., Grodsky S. M., Hernandez R. R. (Yeear) Solar Energy Development and the Biosphere //LETCHER T M, FTHENAKIS V M. A Comprehensive Guide to Solar Energy Systems. Academic Press. 391-405. https://doi.org/10.1016/B978-0-12-811479-7.00020-8.

Nair A. A., A N R., Raj C., McPhillips L. E. (2022). Evaluating the potential impacts of solar farms on hydrological responses. https://dor.org/10.13031/aim.202201262.

Nouvellon Y., Rambal S., Seen D. L., Moran M. S., J. P. Lhomme, Begue A., Chehbouni A. G., Kerr Y. (2000). Modelling of daily fluxes of water and carbon from shortgrass steppes. *Agricultural and Forest Meteorology*, 100, 137-153. https://doi.org/10.1016/S0168-1923(99)00140-9.

Passias D., Källbäck B. (1984). Shading effects in rows of solar cell panels. *Solar Cells*, 11, 281-291. https://doi.org/10.1016/0379-6787(84)90017-6.

Phalane I. (2021). Halfgewonnen Solar PV Facility：hydrological impact assessment.

Poesen J., Nachtergaele J., Verstraeten G., Valentin C. (2003). Gully erosion and environmental change: importance and research needs. *CATENA*, 50, 91-133. https://dor.org/10.1016/S0341-8162(02)00143-1.

Pringle C. M. (2001). Hydrologic connectivity and the management of biological reserves: a global perspective. *Ecological Applications*, 11, 981-998.

Quijano-Baron J., Saco P. M., Rodriguez J. F. (2022). Modelling the effects of above and belowground biomass pools on erosion dynamics. *Catena*, 213, 106123. https://doi.org/10.1016/j.catena.2022.106123.

Rahman A., Farrok O., Haque M. M. (2022). Environmental impact of renewable energy source based electrical power plants: Solar, wind, hydroelectric, biomass, geothermal, tidal, ocean, and osmotic. *Renewable and Sustainable Energy Reviews*, 161, 112279. https://doi.org/10.1016/j.rser.2022.112279.

Randle-Boggis R., White P. C. L., Cruz J., Parker G., Montag H., Scurlock J., Armstrong A. (2020). Realising co-benefits for natural capital and ecosystem services from solar parks: a co-developed, evidence-based approach. *Renewable and Sustainable Energy Reviews*, 125, 109775. https://doi.org/10.1016/j.rser.2020.109775.

Ren Z., Zou F., Yu Y., Wang G., Zhang Z., Fan S., Zhang Z., Sun C. (2021). Daily Climatological Database of China Ground International Exchange Station (V3.0) [Dataset]. China Meteorological Data Service Center. http://data.cma.cn/data/detail/dataCode/A.0012.0001.html.

Rodriguez-Iturbe I. (2000). Ecohydrology: A hydrologic perspective of climate-soil-vegetation dynamies. *Water Resources Research*, 36, 3-9. https://doi.org/10.1029/1999WR900210.

Saco P. M., Mariano M. D. L. H. (2013). Ecogeomorphic coevolution of semiarid hillslopes: Emergence of banded and striped vegetation patterns through interaction of biotic and abiotic processes. *Water Resources Research*, 49, 115-126. https://doi.org/10.1029/2012WR012001.

Saco P. M., Willgoose G. R., Hancock G. R. (2007). Eco-geomorphology of banded vegetation patterns in arid and semi-arid regions.

Hydorlogy and Earth System Sciences, 11, 1717-1730. https://doi.org/10.5194/hess-11-1717-2007.

Shobe C. M. (2022). How impervious are solar arrays? On the need for geomorphic assessment of energy transition technologies. *Earth Surface Processes and Landforms*, 47, 3219-3223. https://dor.org/10.1002/esp.5489.

Smith J., Graves P., Nayak D., Smith P., Perks M., Gardiner B., Miller D., Nolan A., Morrice J., Xenakis S. (2011). Carbon Implications of Windfarms Located on Peatlands–Update of the Scottish Government Carbon Calculator Tool. *Scottish Government, Scotland*,

Souza J., Hooke J. (2021). Influence of seasonal vegetation dynamics on hydrological connectivity in tropical drylands. *Hydrological Processes*, 35, e14427. https://doi.org/10.1002/hyp.14427.

Srivastava A., Saco P. M., Rodriguez J. F., Kumari N., Chun K. P., Yetemen O. (2021). The role of landscape morphology on soil moisture variability in semi-arid ecosystems. *Hydrological Processes*, 35, e13990. https://doi.org/10.1002/hyp.13990.

Sun L., Jiang Y., Guo Q., Ji L., Xie Y., Qiao Q., Huang G., Xiao K. (2021). A GIS-based multi-criteria decision making method for the potential assessment and suitable sites selection of PV and CSP plants. *Resources, Conservation and Recycling*, 168, 105306. https://dor.org/10.1016/j.resconrec.2020.105306.

Tang L. C., Low J. M. (2020). Strategic intent of OBOR: enhancing energy supply resilience. *Journal of Shipping and Trade*, 5, 1-25. https://dor.org/10.1186/s41072-020-0058-1.

van Hateren T., Jongen H., Al-Zawaidah H., Beemster J., Boekee J., Bogerd L., Gao S., Kannen C., van Meerveld I., de Lange S., Linke F., Pinto R., Remmers J., Ruijsch J., Rusli S., van de Vijsel R., Aerts J., Agoungbome S., Anys M., Blanco Ramírez S., van Emmerik T., Gallitelli L., Gesualdo G., Gonzalez Otero W., Hanus S., He Z., Hoffmeister S., Imhoff R., Kerlin T., Meshram S., Meyer J., Meyer Oliveira A., Müller A., Nijzink R., Scheller M., Schreyers L., Sehgal D., Tasseron P., Teuling A., Trevisson M., Waldschläger K., Walraven B., Wannasin C., Wienhöfer J., Zander M., Zhang S., Zhou J., Zomer J., Zwartendijk B. (2022). https://dor.org/10.31223/x5dw7r.

Van Nieuwenhuyse B. (2012). Measuring and Modelling Hydrological Surface Connectivity. *Université catholique de Louvain*.

Wacha K. M., Papanicolaou A., Giannopoulos C. P., Abban B. K., Wilson C. G., Zhou S., Hatfield J. L., Filley T. R., Hou T. (2018). The role of hydraulic connectivity and management on soil aggregate size and stability in the Clear Creek Watershed, Iowa. *Geosciences*, 8, 470. https://doi.org/10.3390/geosciences8120470.

Walston L. J., Li Y., Hartmann H. M., Macknick J., Hanson A., Nootenboom C., Lonsdorf E., Hellmann J. (2021). Modeling the ecosystem services of native vegetation management practices at solar energy facilities in the Midwestern United States. *Ecosystem Services*, 47, 101227. https://dor.org/10.1016/j.ecoser.2020.101227.

Wischmeier W. H., Smith D. D. (1978) Predicting rainfall erosion losses - a guide to conservation planning. Hyattsville, Maryland: USDA, Science and Education Administration.

Wu C., Liu H., Yu Y., Zhao W., Liu J., Yu H., Yetemen O. (2022). Ecohydrological effects of photovoltaic solar farms on soil microclimates and moisture regimes in arid Northwest China: A modeling study. *Science of the Total Environment*, 802, 149946. https://doi.org/10.1016/j.scitotenv.2021.149946.

Yang Q., Huang T., Wang S., Li J., Dai S., Wright S., Wang Y., Peng H. (2019). A GIS-based high spatial resolution assessment of large-scale PV generation potential in China. *Applied Energy*, 247, 254-269. https://doi.org/10.1016/j.apenergy.2019.04.005.

Yavari R., Zaliwciw D., Cibin R., McPhillips L. (2022). Minimizing environmental impacts of solar farms: a review of current science on landscape hydrology and guidance on stormwater management. *Environmental Research: Infrastructure and Sustainability*, https://dor.org/10.1088/2634-4505/ac76dd/meta.

Yetemen O., Istanbulluoglu E., Flores-Cervantes J. H., Vivoni E. R., Bras R. L. (2015). Ecohydrologic role of solar radiation on landscape evolution. *Water Resources Research*, 51, 1127-1157. https://doi.org/10.1002/2014wr016169.

Yu Y., Zhao W., Martinez-Murillo J. F., Pereira P. Loess Plateau: from degradation to restoration. Elsevier. 2020: 140206.

Zhang L., Xue T., Gao F., Wei R., Wang Z., Li H., Wang H. (2021). Carbon Storage Distribution Characteristics of Vineyard Ecosystems in Hongsibu, Ningxia. *Plants*, 10, 1199. https://dor.org/10.3390/plants10061199.

Zhang L., Xue T., Yuan L., Gao F., Hao X., Yang C., Wang L., Han Y., Li H., Wang H. (2022). The effect of vineyard reclamation on

soil properties and microbial communities in desertified land in Hongsibu, Ningxia. *CATENA*, 211, 106002. https://dor.org/10.1016/j.catena.2021.106002.

Zhou X., Istanbulluoglu E., Vivoni E. R. (2013). Modeling the ecohydrological role of aspect-controlled radiation on tree-grass-shrub coexistence in a semiarid climate. *Water Resources Research*, 49, 2872-2895. https://doi.org//10.1002/wrcr.20259.

Zhu Y., Jia X., Shao M. (2018). Loess Thickness Variations Across the Loess Plateau of China. *Surveys in Geophysics*, 39, 715-727. https://doi.org/10.1007/s10712-018-9462-6.

Figure 1. Location map of Hongsibu site, and aerial view of the solar farm in the study site. (a) Location of the experiment site, and meteorologic variables and soil moisture monitoring instruments at the site; (b) three sub-catchments selected in the solar farm; (c) aerial view of the solar farm (dark areas represent photovoltaic arrays).

Figure 2. Schematic diagram of the SOFAR model and feedbacks between sub-models. Blue grid means that there is a photovoltaic array, which is consisted of 20 single photovoltaic panels.

Figure 3. Parameter calibration and validation of the SOFAR model at the Hongsibu site. Blue solid line and dashed line represent simulated and observed soil volumetric water content (VWC), respectively.

Figure 4. Effects of solar farm on soil erosion in comparison to scenarios without a solar farm. (a) Effects of precipitation amount (S1-S3) on soil erosion; (b) effects of precipitation frequency (S4-S6) on soil erosion; (c) effects of landscape relief amplitude (S7-S9) on soil erosion (a negative value of the cumulative soil erosion indicates a downward shift of the ground surface); (d-e) results of soil erosion under scenarios with the installation of a solar farm (ErosionPVs), minus the soil erosion of the scenarios without the installation of a solar farm (ErosionnoPVs). The solid lines represent the results without installation of a solar farm, and the dashed lines represent the results with installation of a solar farm.

Figure 5. Relative changes in soil erosion under the scenarios with the installation of a solar farm, compared to the scenarios without the installation of a solar farm.

Figure 6. Photovoltaic panels' (PVs') enhanced annual runoff, and effects of USFs on hydrologic connectivity (IC value). Dynamics of hydrologic connectivity of the study site affected by the solar farm: (a) to (c) represent results of nine simulation scenarios. The diamonds represent the results with the installation of a solar farm, and the circles represent the results under natural conditions. The blue and pink backgrounds represent the construction period and operation period of the solar farm, respectively.

Figure 7. Map of hydrologic connectivity, average IC values, and average erosion of the three sub-basins. (a) Hydrologic connectivity values for the three sub-basins under Scenario 1; (b) IC values of the three sub-basins; (c) average erosion of the three sub-basins; (d) temporal dynamics of HC for the three sub-basins. The diamonds represent the results with the installation of a solar farm, and the circles represent the results under natural conditions. The blue and pink backgrounds represent the construction period and operation period of the solar farm, respectively.

Figure 8. Relationship between soil erosion, annual runoff, and hydrologic connectivity with the effects of a utility-scale solar farm (USF).

935 **Table 1.** ***Summary of the simulation scenarios***

Scenarios	Description	Relief amplitude (m)	Mean slope (Slope range)	Precipitation (mm yr^{-1})	Rainfall variability (%)
Increased annual precipitation					
Scenario 1 (S1)	Baseline scenario with the data From Hongsibu site	88.43	12.96˚ (0.02˚~55.56˚)	186	465.87
Scenario 2 (S2)	The same geomorphology as S1, but wetter meteorological conditions			377	355.46
Scenario 3 (S3)	The same geomorphology as S1, but wettest meteorological conditions			506	381.60
Increased rainfall variability					
Scenario 4 (S4)	The same annual precipitation amounts and geomorphology as S1, but longer duration of precipitation intermittency	88.43	12.96˚ (0.02˚~55.56˚)	188	593.39
Scenario 5 (S5)	The same annual precipitation amounts and geomorphology as S2, but longer duration of precipitation intermittency			390	560.57
Scenario 6 (S6)	The same annual precipitation amounts and geomorphology as S3, but longer duration of precipitation intermittency			588	533.57
Increased relief amplitude					
Scenario 7 (S7)	Steeper hilly topography, but keeping the meteorological conditions the same as S1	106.79	16.83˚ (0.04˚~67.35˚)	186	465.87
Scenario 8 (S8)	Steeper hilly topography, but keeping the meteorological conditions the same as S2			377	355.46
Scenario 9 (S9)	Steeper hilly topography, but keeping the meteorological conditions the same as S3			506	381.60

936

937 **Table 2.** ***Characteristics of three sub-catchments delineated in the Hongsibu site***

Sub-catchment	Length (m)	Width (m)	Relief amplitude (m)	Mean slope (˚)
T1	800	548	51.4	17.61
T2	547	305	49.8	19.74
T3	700	476	53	13.81

938

939 **Table 3.** ***Model parameter definitions and values estimated for the Wuzhong site***

Definition	Parameter	Grass	Shrub
Soil parameters (units)			
Soil porosity (v v^{-1})	n	0.55	0.55
Active soil depth (mm)	Zr	600	600
Time step (d)	t	1	1
Saturated hydraulic conductivity (cm d^{-1})	K_S	50.8	50.8
Empirical constant	N	2	2
Empirical constant	b	1.62	1.62
Field capacity (v v^{-1})	S_{fc}	0.4	0.4
Bare soil infiltration capacity (mm d^{-1})	I_b	8[a]	5[a]
Vegetation infiltration capacity (mm d^{-1})	I_V	15[a]	13[a]
Incipient stomatal closure (v v^{-1})	S^*	0.14[b]	0.10[b]
Wilting point (v v^{-1})	S_w	0.06	0.042
Hygroscopic point (v v^{-1})	S_h	0.03[c]	0.03[c]
Minimum soil evaporation (mm d^{-1})	E_{min}	0.1	0.1
Photovoltaic panel parameters (units)			
Inclination angle (˚)	β	37.2	
PVs' re-radiation coefficient (%)	η	0.6[d]	
Rainfall interception coefficient (m^2 m^{-2})	K_p	0.3	
Vegetation parameters (units)			
Empirical constant (-)	k_1	0.384[e]	0.384[e]
Specific leaf area index for living biomass (m^2 g^{-1})	C_g	0.0105[e]	0.008[e]
Specific leaf area index for dead biomass (m^2 g^{-1})	C_d	0.011[a]	0.01[a]
Minimum temperature for photosynthesis (℃)	T_{min}	7[e]	5[e]
Optimum temperature for photosynthesis (℃)	T_{opt}	25[e]	25[e]
Minimum root-to-shoot ratio (-)	r_x	0.15	1.05[e]
Maintenance respiration coefficient for aboveground parts (g DM g DM^{-1})	m_a	0.02[e]	0.0008[e]
Growth respiration coefficient for aboveground parts (g DM g DM^{-1})	g_a	0.25[e]	0.01[e]
Maintenance respiration coefficient for belowground parts (g DM g DM^{-1})	m_r	0.0008[e]	0.001[e]
Growth respiration coefficient for belowground parts (g DM g DM^{-1})	g_r	0.2[e]	0.008[e]
Soil erosion (units)			
Density of the sediment (kg m^{-3})	ρ_s	1200	
Porosity of the sediment (v v^{-1})	n_p	0.2[f]	
Empirical coefficient (-)	m_1	0.6[f]	
Empirical coefficient (-)	n_1	0.8[f]	
Maximum diffusion coefficient (m^3 d^{-1} m^{-1})	D_{max}	0.03[f]	
Minimum diffusion coefficient (m^3 d^{-1} m^{-1})	D_{min}	0.01[f]	
Maximum erodibility for bare soil (-)	β_b	0.04[f]	
Erodibility for covered soil (-)	β_v	0.02[f]	
Minimum erodibility for soil (-)	β_{min}	0[f]	

940 Note: The values labeled with 'a' through 'f' are estimated through a genetic algorithm (GE) based on the initial values or ranges
941 reported in literatures: [a] Yetemen et al. (2015), [b] Istanbulluoglu et al. (2012), [c] Laio et al. (2001), [d] Hu et al. (2016), [e] Nouvellon et al.
942 (2000), and [f] Saco and Mariano (2013).
943

Figure 1.

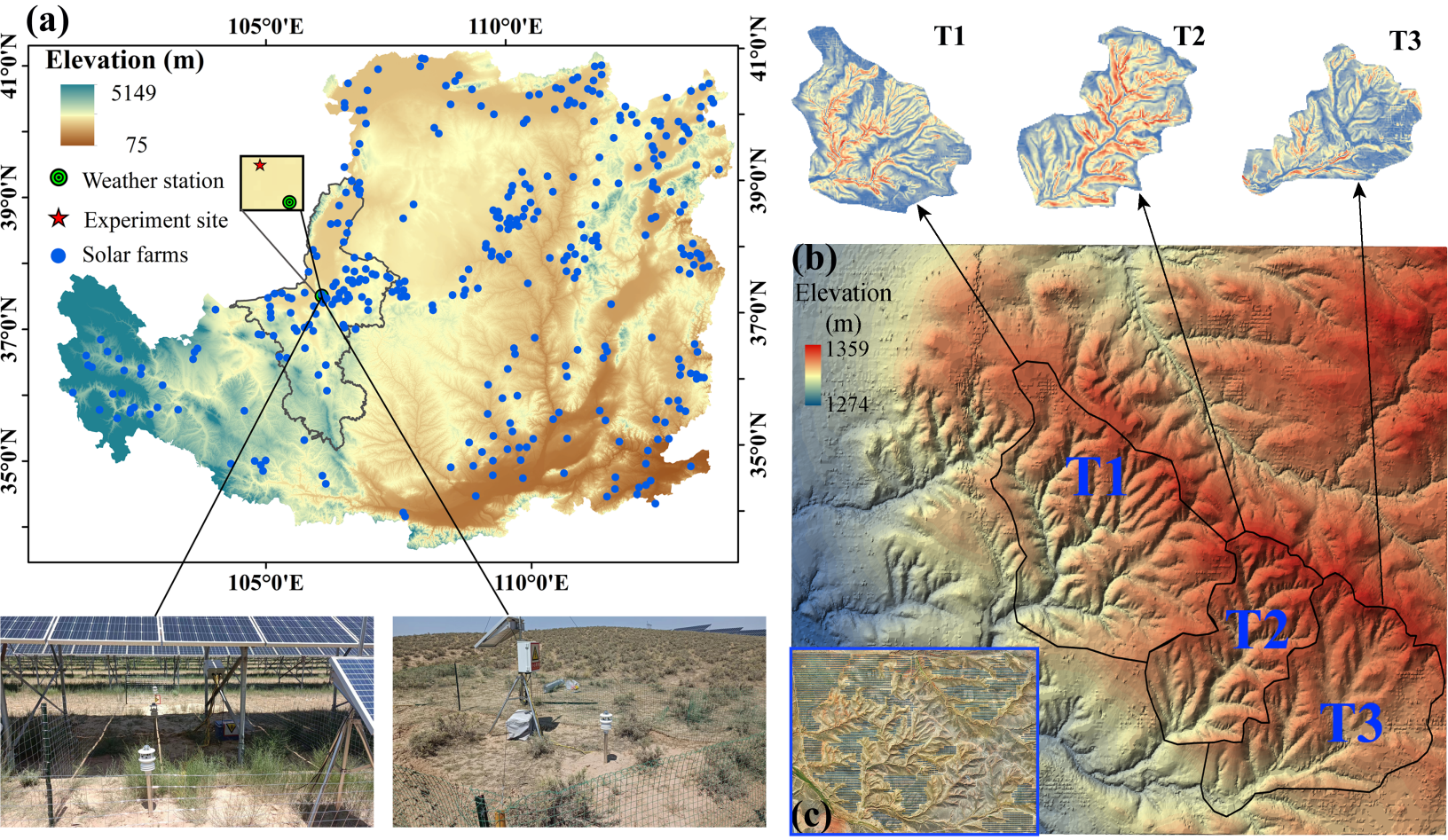
(a)
105°0'E
110°0'E
41°0'N
39°0'N
37°0'N
35°0'N
Elevation (m)
5149
75
Weather station
Experiment site
Solar farms
T1
T2
T3
(b)
Elevation
(m)
1359
1274
T1
T2
T3
(c)

Figure 2.

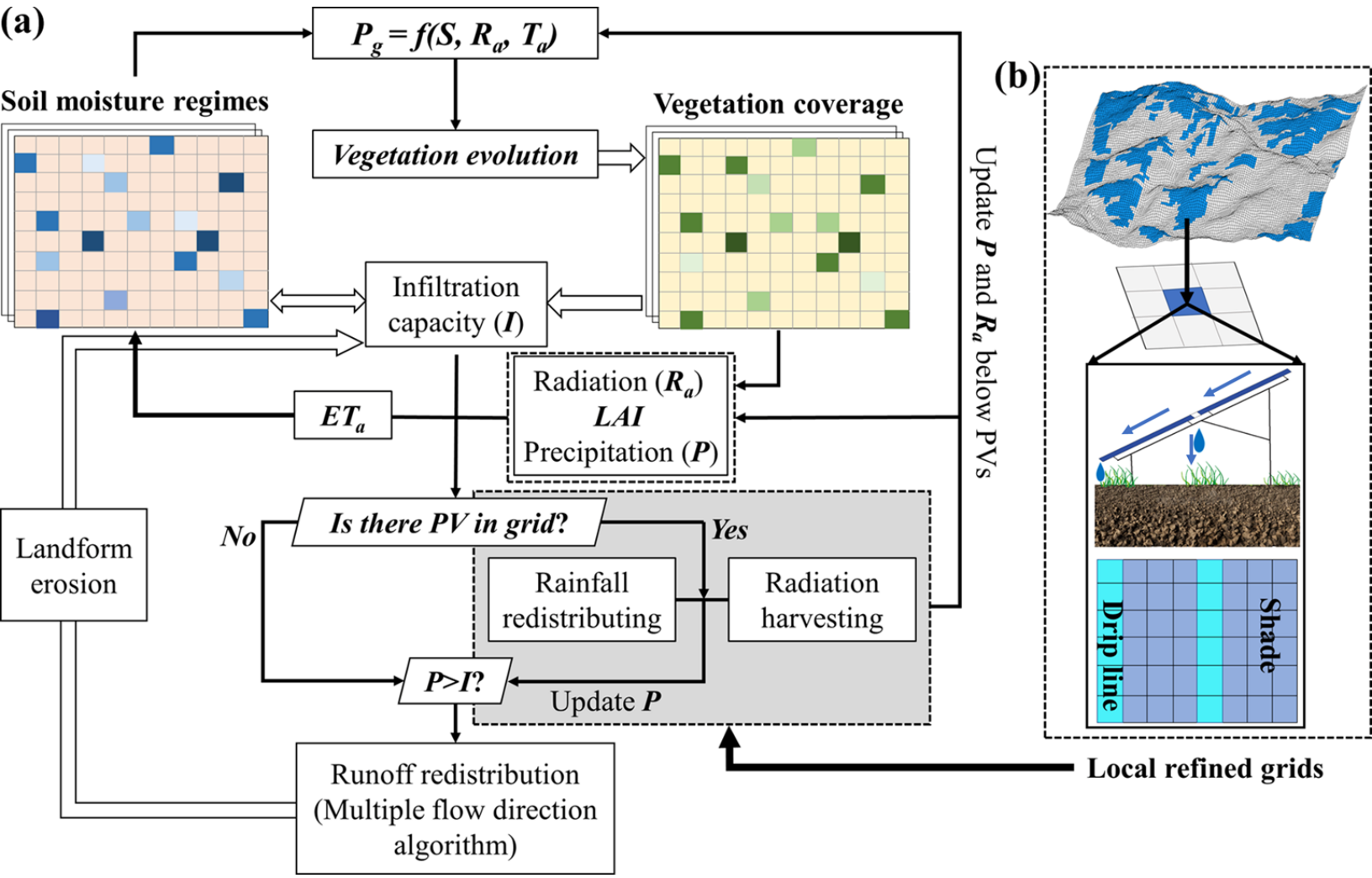
(a)
$P_g = f(S, R_a, T_a)$
Soil moisture regimes
Vegetation coverage
Vegetation evolution
Infiltration capacity (I)
ET_a
Radiation (R_a)
LAI
Precipitation (P)
Landform erosion
Is there PV in grid?
No
Yes
Rainfall redistributing
Radiation harvesting
$P>I$?
Update P
Runoff redistribution (Multiple flow direction algorithm)
Update P and R_a below PVs
(b)
Drip line
Shade
Local refined grids

Figure 3.

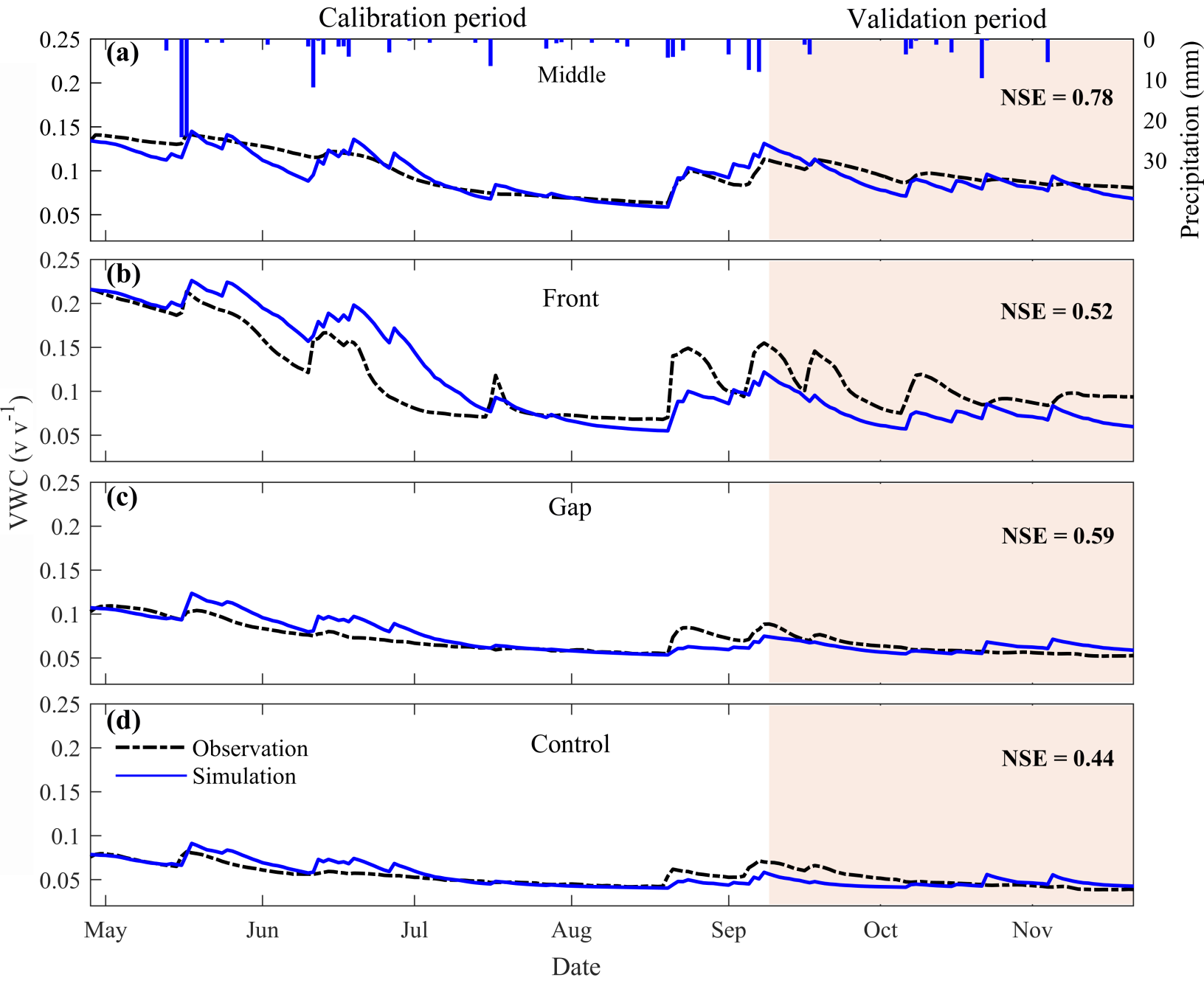
Calibration period
Validation period
(a)
Middle
NSE = 0.78
(b)
Front
NSE = 0.52
(c)
Gap
NSE = 0.59
(d)
Control
NSE = 0.44
Observation
Simulation
VWC (v v-1)
Precipitation (mm)
0.25
0.2
0.15
0.1
0.05
0
10
20
30
May
Jun
Jul
Aug
Sep
Oct
Nov
Date

Figure 4.

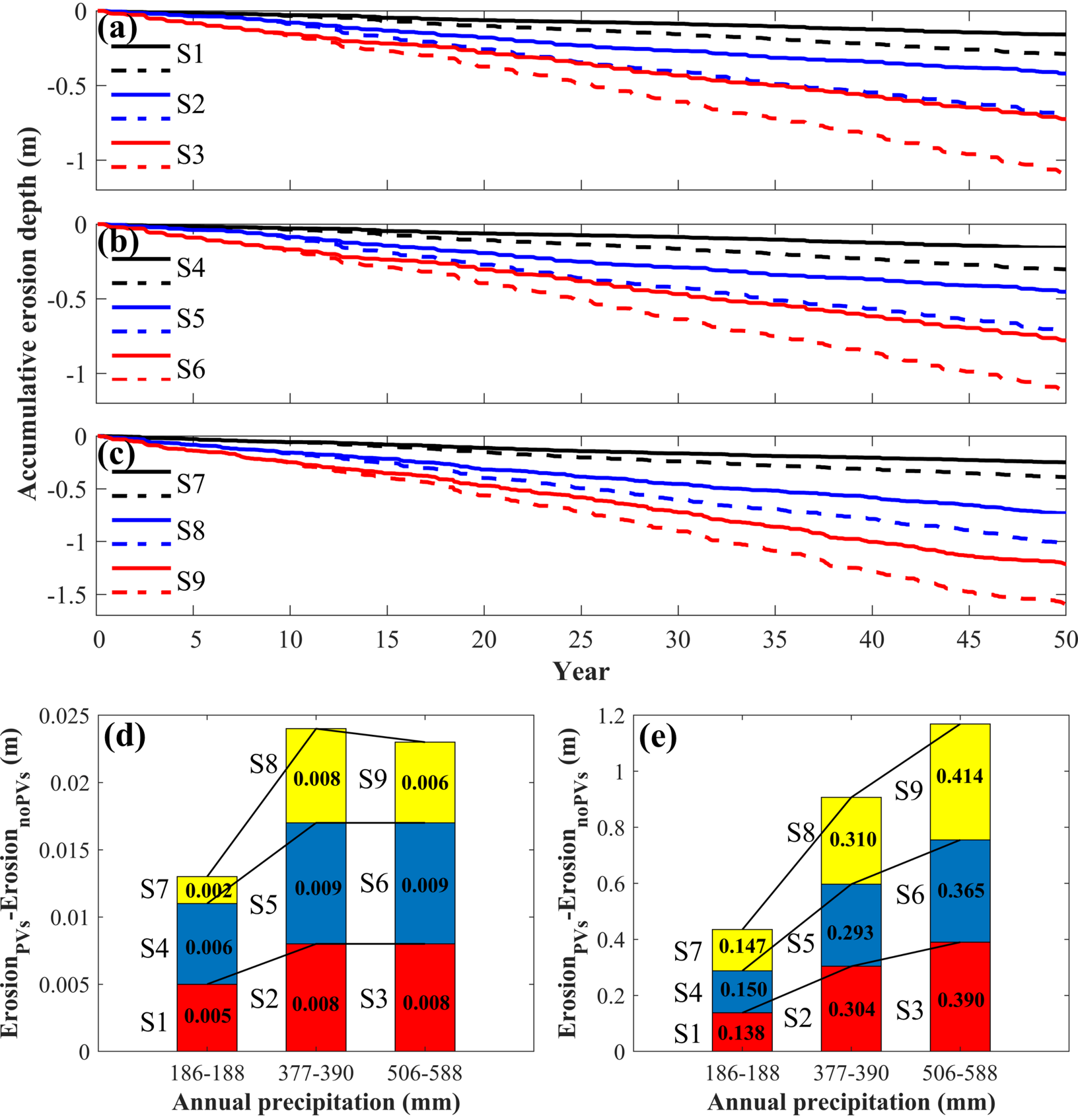
(a)
S1
S2
S3
(b)
S4
S5
S6
(c)
S7
S8
S9
Accumulative erosion depth (m)
0
-0.5
-1
-1.5
0
5
10
15
20
25
30
35
40
45
50
Year

(d)
S1
S2
S3
S4
S5
S6
S7
S8
S9
0.005
0.008
0.008
0.006
0.009
0.009
0.002
0.008
0.006
Erosion$_{PVs}$-Erosion$_{noPVs}$ (m)
0.025
0.02
0.015
0.01
0.005
0
186-188
377-390
506-588
Annual precipitation (mm)

(e)
S1
S2
S3
S4
S5
S6
S7
S8
S9
0.138
0.304
0.390
0.150
0.293
0.365
0.147
0.310
0.414
Erosion$_{PVs}$-Erosion$_{noPVs}$ (m)
1.2
1
0.8
0.6
0.4
0.2
0
186-188
377-390
506-588
Annual precipitation (mm)

Figure 5.

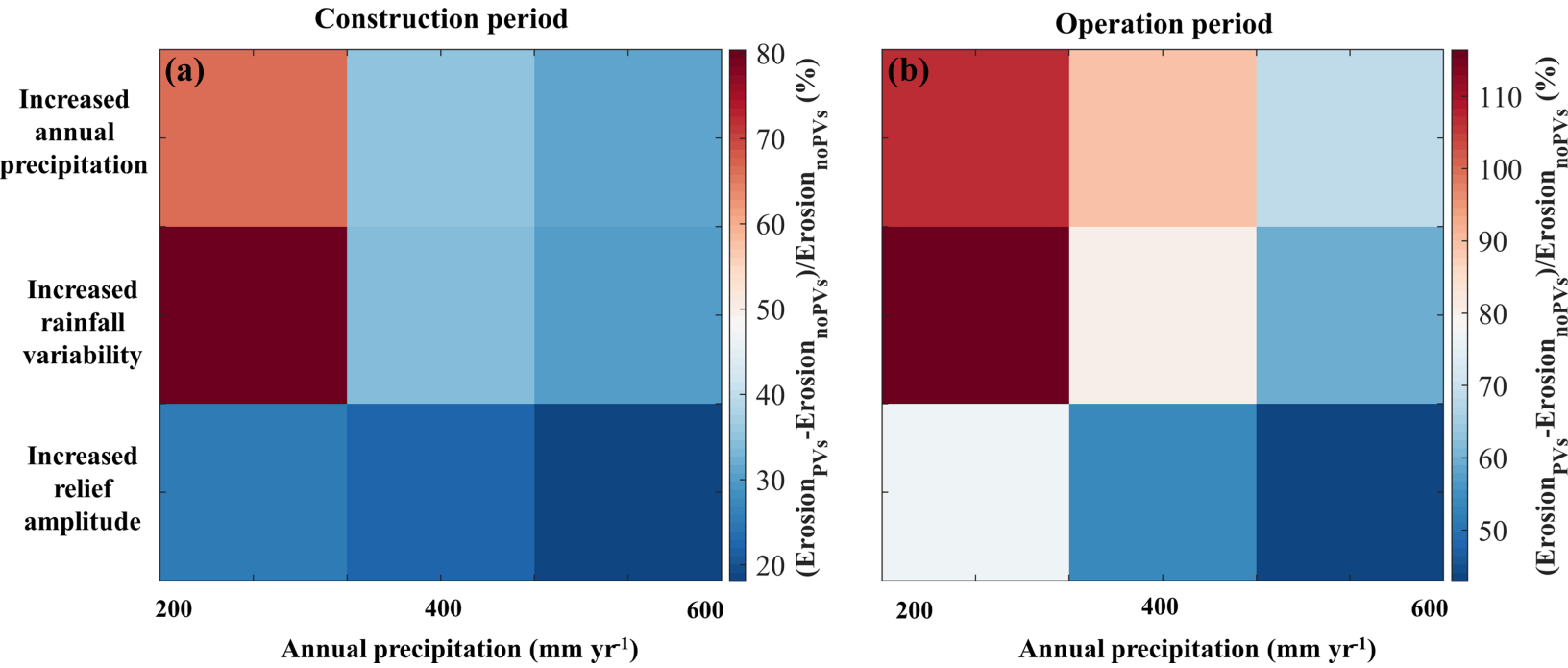
Construction period
Operation period
(a)
(b)
Increased annual precipitation
Increased rainfall variability
Increased relief amplitude
200
400
600
Annual precipitation (mm yr-1)
80
70
60
50
40
30
20
110
100
90
80
70
60
50
(Erosion_PVs-Erosion_noPVs)/Erosion_noPVs (%)

Figure 6.

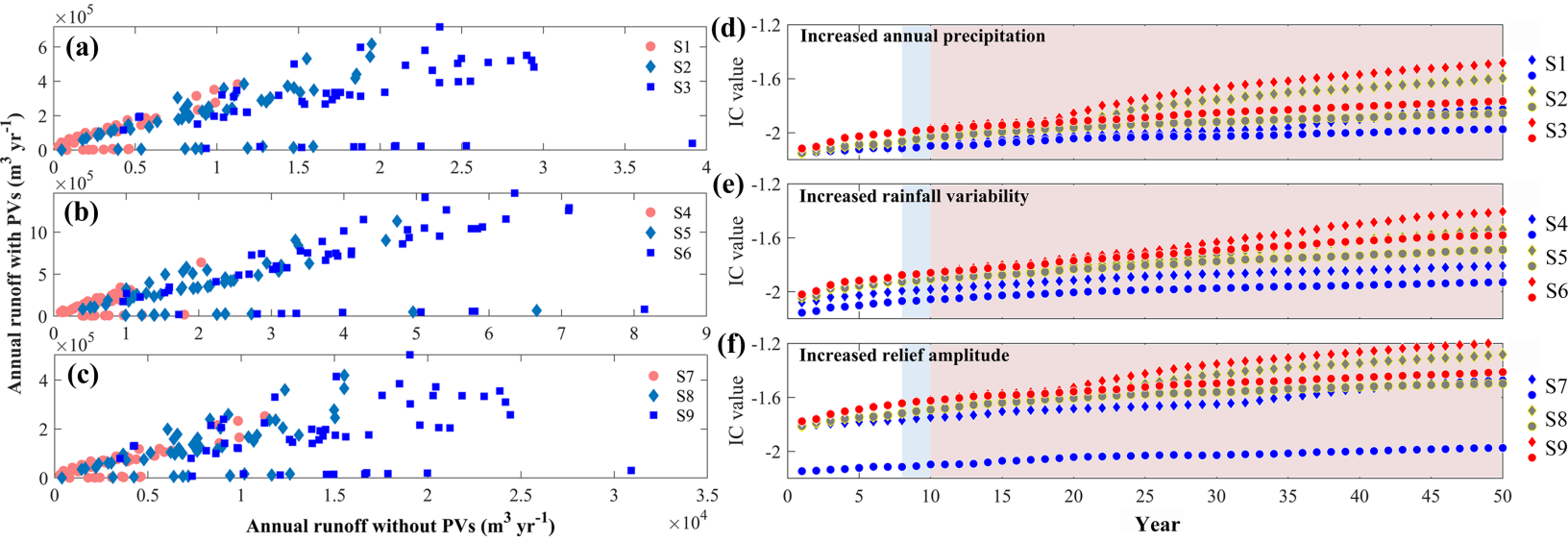
(a)
(b)
(c)
(d)
(e)
(f)
S1
S2
S3
S4
S5
S6
S7
S8
S9
Annual runoff with PVs (m3 yr-1)
Annual runoff without PVs (m3 yr-1)
×10^5
×10^4
IC value
Year
Increased annual precipitation
Increased rainfall variability
Increased relief amplitude

Figure 7.

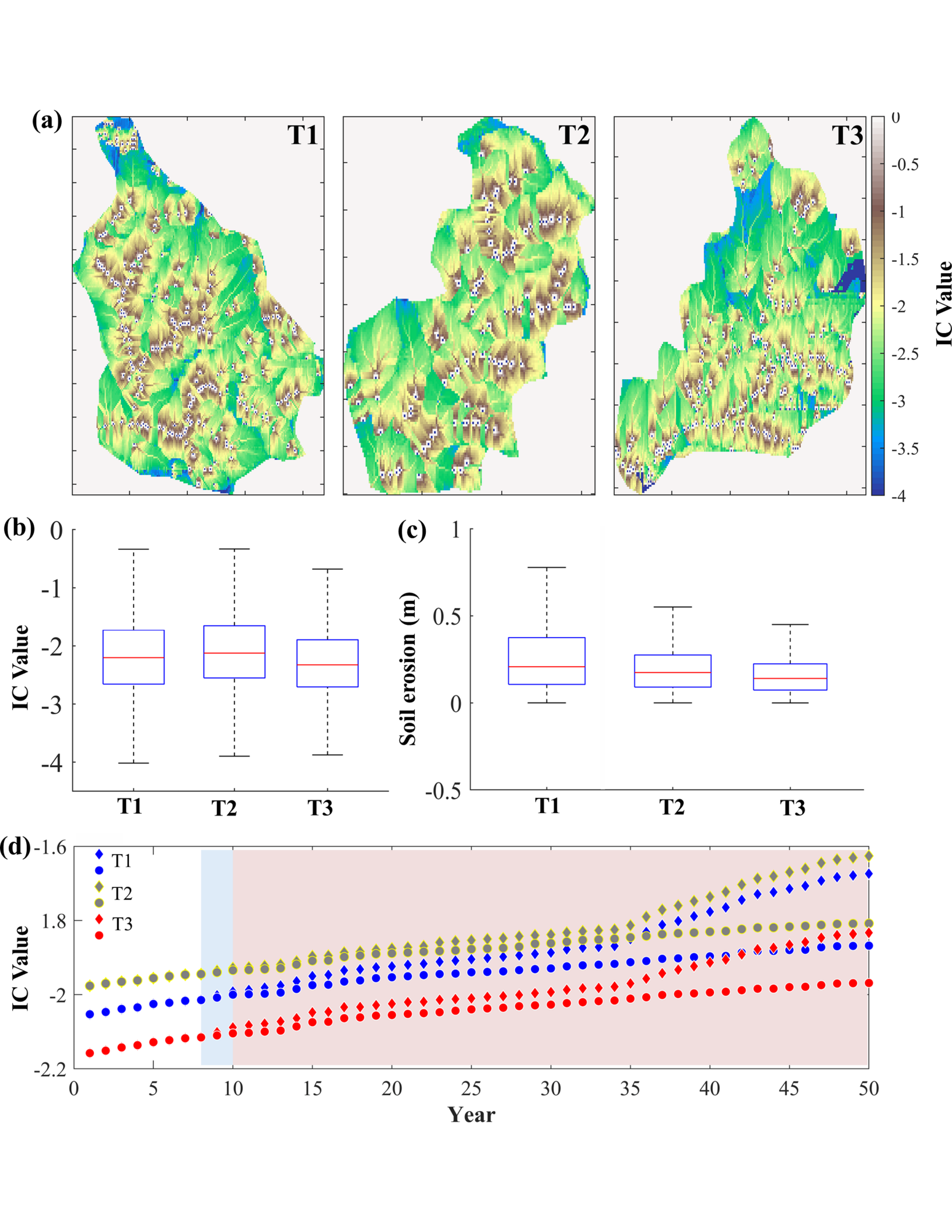
(a)
T1
T2
T3
0
-0.5
-1
-1.5
-2
-2.5
-3
-3.5
-4
IC Value
(b)
IC Value
0
-1
-2
-3
-4
T1
T2
T3
(c)
Soil erosion (m)
1
0.5
0
-0.5
T1
T2
T3
(d)
IC Value
-1.6
1.8
-2
-2.2
T1
T2
T3
0
5
10
15
20
25
30
35
40
45
50
Year

Figure 8.

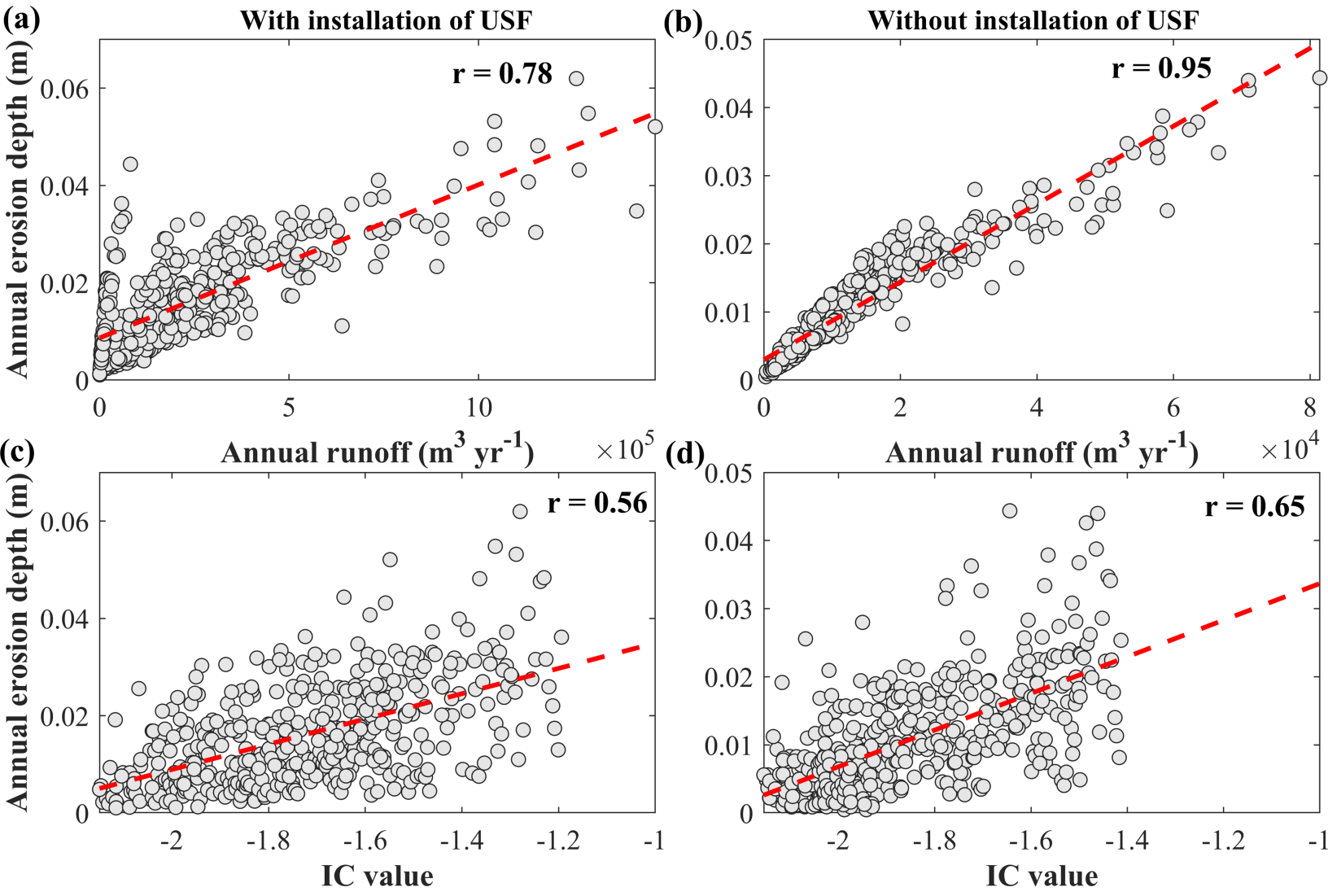
(a)
With installation of USF
r = 0.78
Annual erosion depth (m)
0
0.02
0.04
0.06
0
5
10
(b)
Without installation of USF
r = 0.95
0
0.01
0.02
0.03
0.04
0.05
0
2
4
6
8
(c)
Annual runoff (m3 yr-1)
×10^5
r = 0.56
Annual erosion depth (m)
0
0.02
0.04
0.06
-2
-1.8
-1.6
-1.4
-1.2
-1
IC value
(d)
Annual runoff (m3 yr-1)
×10^4
r = 0.65
0
0.01
0.02
0.03
0.04
0.05
-2
-1.8
-1.6
-1.4
-1.2
-1
IC value